Master's thesis

Factory acceptance analysis of fission and ionisation microchambers for IFMIF-DONES

Pablo Ortega Flores
July 2023

UNIVERSIDAD DE GRANADA

Author: Pablo Ortega Flores
Department: Electronics and Computer Technology
University of Granada

UNIVERSIDAD
DE GRANADA

Factory acceptance analysis of fission and ionisation microchambers for IFMIF-DONES

Report presented as part of the requirements for obtaining the title of Master's Degree in Physics: Radiation, Nanotechnology, Particles and Astrophysics at the University of Granada.

Carried out

Pablo Ortega Flores

Mentored by

Santiago Becerril Jarque

Andrés Roldán Aranda

Contents

List of Figures

*List of Acronyms

Acronym	**Full Form**
DEMO	DEMOnstration power plant
FC	Fission Chambers
FMC	Fission Micro Chambers
HFTM	High Flux Test Module
IC	Ionization Chambers
IMC	Ionization Micro Chambers
ID	IDentity
IFMIF-DONES	International Fusion Materials Irradiation Facility - Demo Oriented NEutron Source
MFC	Micro Fission Chambers
MIC	Micro Ionization Chambers
MFTM	Medium Flux Test Module
RIG	Radiation Instrumentation Group
RX	X-Ray
SPN	Self Powered Neutron
SPND	Self Powered Neutron Detectors
STUMM	Start-Up Monitoring Module
STUMM-PROTO	Start-Up Monitoring Module PROTOtype
UGR	University of GRanada

1 Abstract

This work addresses the study of the response of ionization chambers and fission chambers that will be used to characterize gamma and neutron radiation passing through the STUMM-PROTO device. These investigations are carried out in a pre-irradiation stage of samples at the International Facility for Material Irradiation for Neutron Source Oriented to DEMO Fusion (IFMIF-DONES).

The main results of experimental tests conducted by the manufacturer before distributing the detectors have been examined, leading to conclusions about individual and general properties. It has been observed that electrical properties, such as leakage current and electrical resistance, are affected by temperature. Additionally, a direct relationship between the sensitive volume of the detector and the I-V characteristic has been identified. Regression models have been analyzed and developed to establish the relationship between radiation intensity and ionization intensity.

Keywords: Detectors, fission chambers, ionization chambers, IFMIF-DONES, data analysis.

En este trabajo, se ha abordado el estudio de la respuesta de las cámaras de ionización y las cámaras de fisión que serán utilizadas para caracterizar la radiación gamma y neutrónica que atravesará el dispositivo STUMM-PROTO. Estas investigaciones se llevan a cabo en una etapa previa a la irradiación de muestras en la Instalación Internacional de Irradiación de Materiales para Fuentes de Neutrones Orientadas a la Fusión DEMO (IFMIF-DONES).

Se han examinado los principales resultados de las pruebas experimentales realizadas por el fabricante antes de distribuir los detectores, y se han obtenido conclusiones sobre propiedades individuales y generales. Se ha observado que propiedades eléctricas, como la corriente de fuga y la resistencia eléctrica, se ven afectadas por la temperatura. Además, se ha identificado una relación directa entre el volumen sensible del detector y la característica I-V. Se han analizado y desarrollado modelos de regresión para la relación entre la intensidad de la radiación y la intensidad de ionización.

Palabras clave: Detectores, cámaras de fisión, cámaras de ionización, IFMIF-DONES, Análisis de datos.

2 Introduction

Fission and ionisation microchambers are radiation sensors used in fission nuclear power plants for monitoring and diagnosing thermal neutron fluxes in the relevant areas of the reactor. In IFMIF-DONES such detectors will be used in a different range, focusing on energies above 1 MeV (fast neutrons). In addition, the high spatial density in the arrangement of these sensors has meant that they have had to be custom-developed with a miniaturised size.

This type of neutron sensor has several constraints to take into account:

- To generate a current proportional to the neutron flux, they use a few micrograms of uranium which, on receiving the neutron, generates a particle that interacts with a gas inside it, which in turn releases an electron, which can be measured with an electrometer.
- The small amount of uranium, according to radioprotection standards, makes it necessary to maintain a storage and safekeeping protocol that makes it impossible for unqualified operators to tamper with it.
- To excite the sensor without activating it, X-rays are used to ionise the gas that triggers the generation of electrons. In this way, the sensor can be partially characterised.
- The level of current they generate is very small, in the order of 10^{-9} A (nA).
- In addition, if the sensor were exposed to the neutron flux, the metallic parts of the sensor would be permanently activated so that its use would not be permitted by radiation protection regulations.

Taking these limitations into account, this master's thesis proposes a detailed study of the acceptance procedure to which the sensors have been subjected. The aforementioned acceptance process has been carried out at the manufacturer's facilities, since the UGR does not have the X-ray generator facilities in operation. The acceptance process consisted of carrying out different tests to check, using only X-rays, that the neutron sensor manufactured for the radiation levels expected in IFMIF-DONES would behave in a linear way under these circumstances.

The interest of the work lies in the fact that the neutron sensors to be studied have been specially manufactured for IFMIF-DONES and there are no others of such a small size as the ones proposed to be characterised. The data set obtained from measurements at the Photonis manufacturer's facility in France has been documented by hand for each of the sensors measured. It is necessary to convert all data written in the acceptance documents into digital format in order to be able to manipulate them numerically.

2.1 Objetives

- Develop a theoretical study of the mode of operation of sensors, in pulsed mode and continuous mode from the literature.

- Follow up on the acceptance plan developed at the manufacturer's site for these sensors and establish the measurement protocol to be carried out at the UGR when the X-ray generator is operational again.
- To analyse all the data obtained during the acceptance process where an X-ray source has been used to excite the sensors and not to generate activation in the metals that make up the sensors. Comparisons will be made of the behaviour of the set of sensors.
  - **Test 1:** I (current) vs. V (voltage) characteristic [current generated by the sensor for a range of bias voltage, at an X-ray radiation level] of the detectors. Description of the procedure/equipment used during the measurements. Development of a Python algorithm to process the data from the different neutron sensors.
  - **Test 2:** I(current) vs. X-ray flux characteristic (current generated by the sensor, for a bias voltage, over a range of X-ray flux). Description of the procedure/equipment used during the measurements. Realisation of an algorithm in Python that performs the processing of the data from the different neutron sensors.
  - **Test 3:** Attenuation as a function of frequency. Procedure for characterisation of the coaxial cable linking the sensors to the data acquisition system. The measurement setup-up proposed by the manufacturer shall be analysed and the circuit equivalent of the experiment shall be studied in order to analyse the results provided by the manufacturer.
  - **Test 4:** Impedance measurement using a reflectometer. In order to detect problems in the high insulation mineral dielectric coaxial cable, it is proposed to use the reflectometry technique and for this purpose, the procedure to be carried out and how the data would be processed once the manufacturer sends the rest of the sensors will be detailed.
  - **Test 5:** Measurement of the leakage current in the detector's mineral cable, both at room temperature and at 350°C: This is a key parameter for the good performance of the detector, which generates modest current signals, around tens of nA minimum. If the insulation is not of very high quality, the leakage currents can be so high that they mask the signal produced in the detector.
- Study to determine the optimum polarization voltage of the different microchambers.

2.2 Context

The IFMIF-DONES facility is a project aimed at producing a powerful stream of neutrons with a fusion-like spectrum, and is designed to test sample materials up to a dose corresponding to the expected end of life of DEMO. This stream of neutrons will be generated by one deuteron accelerators (and it is expected to be expanded to two accelerators in the future), which will be used to target a liquid lithium screen as shown in the figure 1.

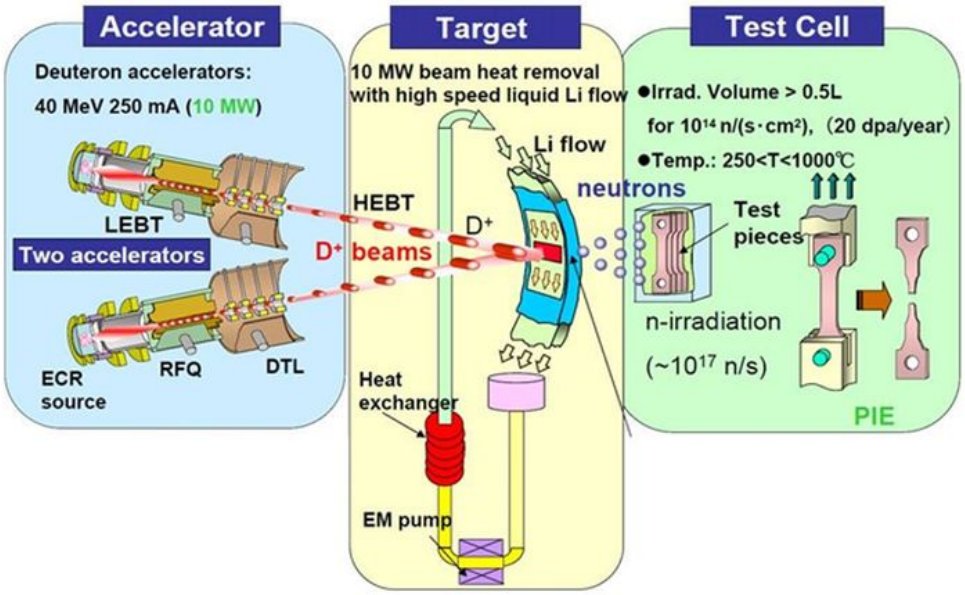

Figure 1: Neutron flux creation line at IFMIF-DONES. [20]

The facility is based on a 40 MeV, 125 mA (each acelerator) continuous wave deuteron accelerator, which will produce a beam with an average power of 5 MW. The beam will be shaped with a rectangular size of approximately 20 cm x 5 cm, and will hit a liquid lithium screen target flowing at 15 m/s. This process will generate a flux of neutrons of 10^{14} $\frac{n}{cm^2\ s}$, with a broad peak at 14 MeV, through stripping nuclear reactions. These reactions will reproduce the expected conditions of fusion power plants.

A more general schematic can be seen in Figure 2, which shows not only an accelerator but also the complexity of the facility, which includes test facilities, post-irradiation facilities, a system for purifying the lithium that gradually loses purity, a system for extracting heat from the liquid lithium among others.

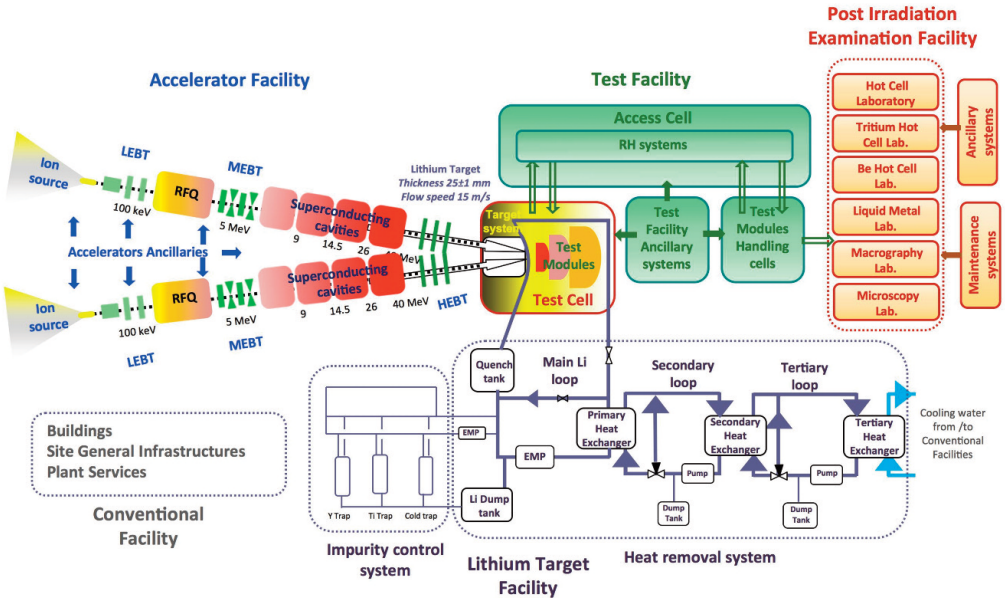

Figure 2: Schematic of the main facilities of the neutron irradiation line at IFMIF-DONES. [5]

The building envisaged to house this facility is shown in figure 3.

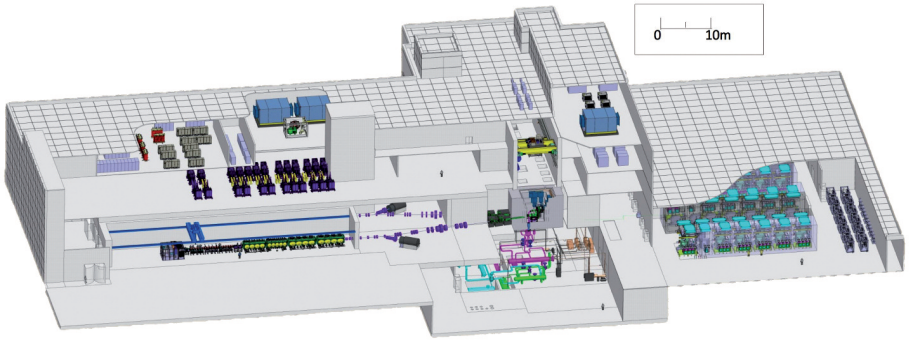

Figure 3: Planned building where all facilities will be installed at IFMIF-DONES. [5]

It can be difficult to monitor the neutron flux during irradiation in the test Cell due to the following reasons:

- Long-term irradiation lasting for a year is expected, during which there will be no access to the cell for maintenance or monitoring.
- The high neutron flux of 10^{14} $\frac{n}{cm^2\ s}$ on the samples with temperatures of 250-550°C, poses a serious challenge for any type of detector.

For this reason, the behaviour of the detectors will be studied before the characterisation of the radiation beam [9].

2.2.1 High-Flux Test Module

The test cell of IFMIF is a protected volumen where the lithium source and test modules are located. The available irradiation volume has been divided into a high-flux test module (HFTM) for structural materials irradiation; a medium-flux test module (MFTM) for tritium release and creep fatigue experiments as well as low flux regions. The reference design of the HFTM consists of twelve irradiation rigs, which contain the test specimens. Figure 4 shows a detail of the test cell, including the test modules and the lithium target (for futher explanation see [11] and [10]).

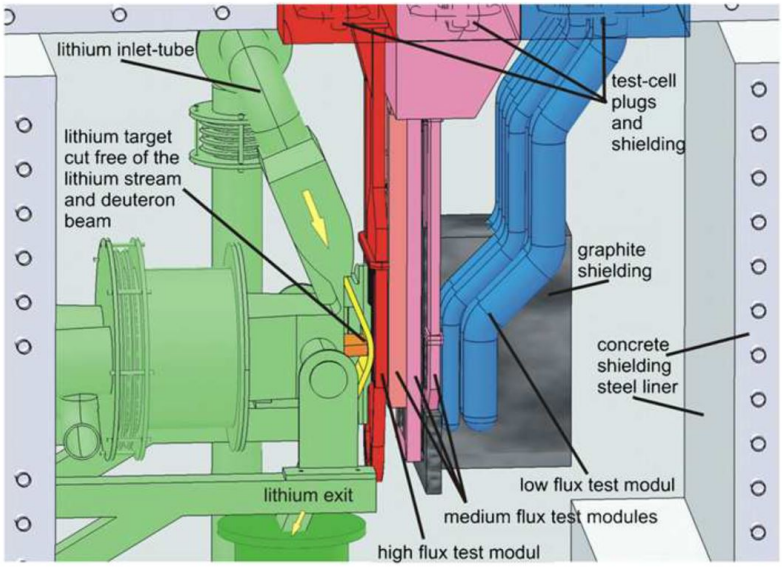

Figure 4: Schematic showing a close-up view of the test cell's interior, which features the test modules and the lithium target. [8]

2.2.2 Start-Up Monitoring Module

To understand the effects of neutron radiation on the materials being tested, the experiment must be conducted with a full understanding of the characteristics of the neutron beam in which the materials will be submerged. This need to understand the neutron beam is justified when seeking to establish a cause-and-effect relationship for irradiated materials. To achieve this, there will be an initial phase of neutron beam and accompanying photon beam (among other types of radiation) characterization, generated by the nuclear reaction between deuterium and lithium. A set of detectors, including ionization chambers (sensitive to photons) and fission chambers (sensitive to neutrons and photons), will be installed in a module called STUMM figure 5. The STUMM module aims to be as similar as possible to the HFTM, in order to know the neutron and photon flux in a similar geometry and with similar materials to those in the test materials when they are exposed to the radiation beam.

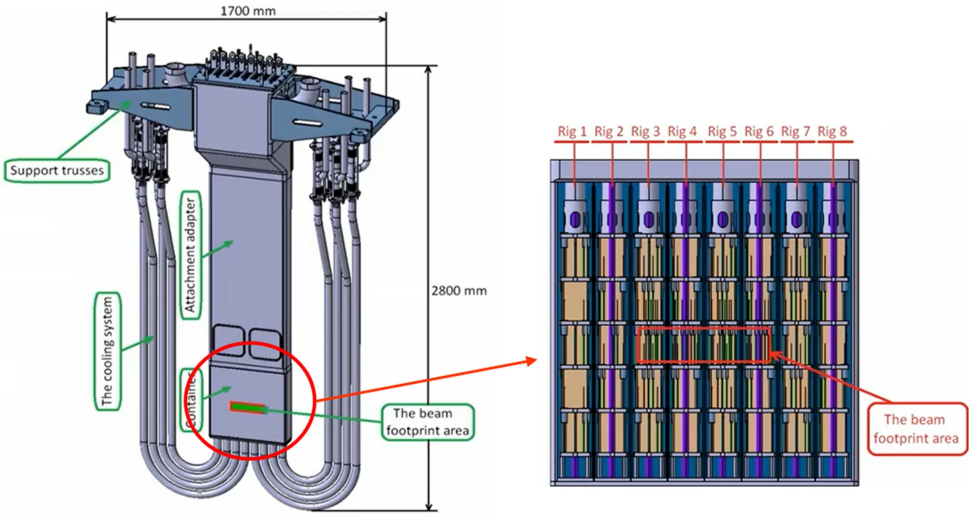

Figure 5: Configuration of the IFMIF-DONES STUMM. [6]

The STUMM will be equipped with various types of detectors, including miniaturized ionization chambers (IC) and fission chambers (FC). The total number of IC and FC units will reach 120 between the two types, and they will be responsible for detecting photons and neutrons with energies on the order of MeV (the neutrons produced in nuclear fusion are approximately 14 MeV). The fact that the energy of the neutrons is on the order of MeV presents a problem, as FC ans IC are designed to detect neutrons produced in nuclear reactors where the neutrons have energies lower than 1 MeV (usually thermal neutrons, with energies on the order of meV).
Because the expected energy of the neutrons produced in IFMIF-DONES is 9 orders of magnitude higher than the energy of thermal neutrons, it is necessary to verify the proper functioning of the IC and FC when the energy of the particles they will detect exceeds by several orders of magnitude the average energy for which they were designed.

2.2.3 Start-Up Monitoring Module - Prototipe

The testing phase of the IC and FC will be carried out in a module that will be very similar to the STUMM, with the aim of studying the behavior of the detectors under the most similar circumstances possible to when the neutron and photon beams are characterized.

The new module that will be used to verify the proper functioning of the detectors is called the Start-Up Monitoring Module - Prototype (STUMM-PROTO), and it will house a quarter of the IC and FC units that the STUMM will use to characterize the neutron and photon beams. Specifically, it will house:

- 15 gamma ionization chambers.
- 15 Fission chambers:
  - 9 current mode ^{238}U FC
  - 3 current mode ^{235}U FC
  - 3 pulse mode ^{238}U FC

The STUMM-PROTO will have fewer detectors than the STUMM, but it will be equally densely populated with detectors, which means that a portion of its volume will be unoccupied (empty). This is done to study the behavior of detectors when they are very close to each other (which is how they will be in the STUMM) and to be able to detect unwanted interactions between them in case they occur, as they would then give a spurious contribution in the output signal.

3 Theoretical framework

3.1 Simplified detector model

We start by considering an imaginary detector that is exposed to some form of radiation. Initially, we concentrate on the impact of a solitary particle (or quantum of radiation) within the detector. This could be an individual gamma-ray photon or a single alpha particle, for instance. For the detector to react, the radiation must interact through one of the mechanisms in which it interacts with matter. In practical scenarios, the time it takes for the interaction (or stopping time) is extremely short, usually in the order of a few nanoseconds in gases or a few picoseconds in solids. As a result, the deposition of energy from the incoming particle can be considered instantaneous.

The interaction of radiation with a detector results in the generation of electric charge within the active volume of the detector. Our simplified detector model assumes that this charge Q is generated instantaneously at time $t = 0$ due to the interaction of a single particle. Next, this charge must be collected to form the basic electrical signal. Typically, this is achieved through the application of an electric field within the detector, causing the positive and negative charges to move in opposite directions. The time required for the whole electric charge to be collected varies between detectors due to differences in charge carrier mobility and the average distance traveled to reach collection electrodes. Collection times can range from a few nanoseconds in semiconductor diode detectors to several milliseconds in ion chambers.

To model the response of a detector to radiation, we start with a simplified detector that produces a current when exposed to a single particle. This current lasts for the duration of the charge collection time, which varies depending on the detector type. An example of the current response over time is shown in figure 6, with t_c indicating the charge collection time.

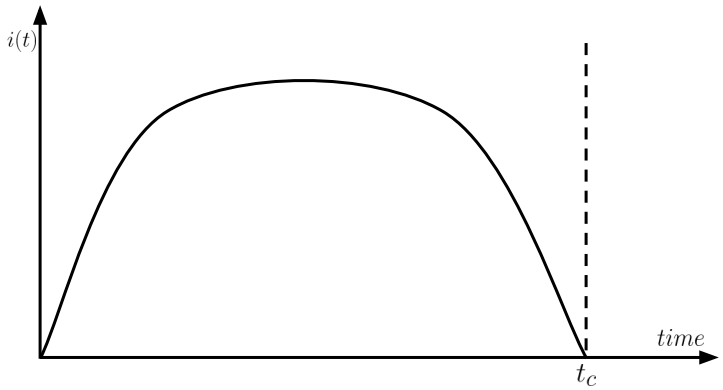

$$Q = \int_0^{t_c} i(t)\, dt \quad (1)$$

Figure 6: Intensity across the detector as a function of the time of a single detection.

The total charge Q produced in the interaction must be equal to the integral of the current over the entire duration of the electric signal (1).

In practical scenarios, multiple particles interacts with the detector over a period of

time. At high irradiation rates, the resulting current may be a combination of currents from multiple interactions occurring simultaneously. However, for the purpose of this discussion, we assume that the irradiation rate is low enough that each interaction generates a distinguishable current pulse. The magnitude and duration of each pulse depend on the type of interaction, and a representation of the current that flows in the detector at a particular moment can be illustrated as depicted in figure 7.

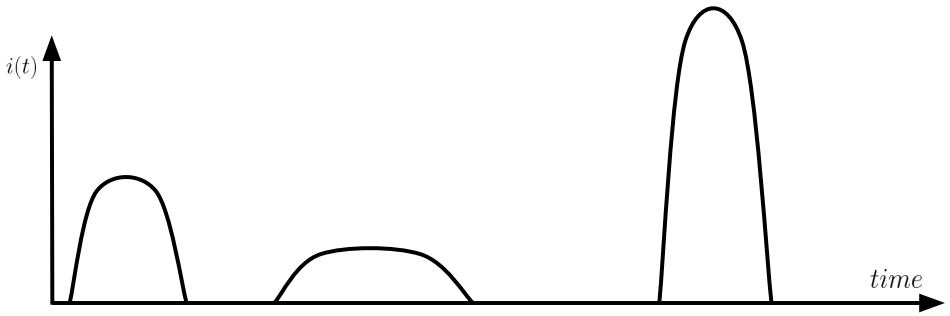

Figure 7: Intensity across the detector as a function of time of multiple detections.

It is crucial to keep in mind that the time intervals between current pulses are randomly distributed due to the fact that the arrival of radiation quanta follows Poisson statistics, which is a stochastic process.

3.2 Modes of detector operation

We can now introduce a fundamental distinction between three general modes of operation of radiation detectors. Those are: pulse mode, current mode, and mean square voltage (MSV) mode, also known as Campbell mode. The most commonly used mode is pulse mode, but current mode is also widely used. MSV mode is only used in specialized applications due to its unique characteristics. Despite their operational differences, all three modes depend on the sequence of current pulses generated by the detector. Since the detectors relevant to this work are intended to be used in pulsed and current mode, only these will be presented.

Pulse mode operation records each individual interaction of radiation in the detector. In this mode, the measurement equipment measures the time integral of each burst of current or the total charge Q, which is directly related to the energy deposited in the detector. This mode is essential for detectors used in radiation spectroscopy to measure the energy of individual radiation quanta.

In certain situations, a more straightforward method may be appropriate for the measurement needs: only pulses above a certain threshold are detected by the measurement equipment, regardless of the charge value Q. This technique is commonly referred to as pulse counting. It can be advantageous in numerous applications where the focus is solely on the radiation intensity, rather than the energy distribution of the incoming radiation.

When the event rate becomes very high, using pulse mode operation may become difficult or impossible. The time between events may be too short to analyze or the current

pulses from different events may overlap. In these situations, alternative measurement techniques can be used that respond to the time average taken over many events. This leads to the two other modes of operation: current mode and mean square voltage (MSV) mode.

3.2.1 Current mode

In the diagram provided below, we illustrate the connection of a current measurement device, such as an ammeter, to the output terminals of a radiation detector.

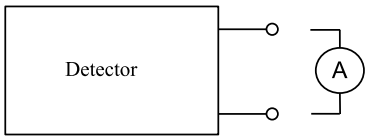

Figure 8: Detector and Amperemeter

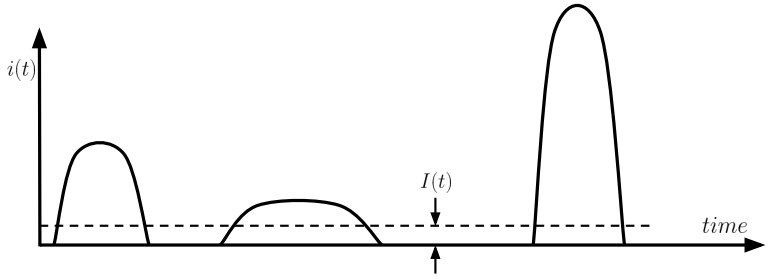

Figure 9: Multiple detections and the current recorded by the amperemeter

Assuming that the measuring device has a constant response time T, the recorded signal from a series of events will be a time-varying current represented by the following expression:

$$I(t) = \frac{1}{T}\int_{t-T}^{t} i(t')\,dt' \tag{2}$$

Due to the relatively long response time T of the measuring device compared to the average time between individual current pulses from the detector,the effect is to average out many of the fluctuations in the intervals between individual radiation interactions, and to record an average current that depends on the product of the interaction rate and the average charge per interaction. In current mode operation, this time-averaged current from the individual bursts becomes the fundamental signal that is recorded.

At any given moment, there is a statistical uncertainty present in this signal caused by the random variations in the arrival time of events. Consequently, selecting a larger value for T will reduce the statistical fluctuations in the signal. However, it will also result in a slower response to rapid changes in the rate or characteristics of the radiation interactions.

The average current is given by the product of the event rate and the average charge produced per event.

$$I_0 = rQ = r\frac{E}{W}q \tag{3}$$

where;

- $r =$ event rate
- $Q = Eq/W =$ charge produced for each event
- $E =$ average energy deposited per event

- W = average energy required to produce a unit charge pair (e.g., electron-ion pair)
- $q = 1.6 \times 10^{-19}$C

For steady-state irradiation of the detector, the average current can be expressed as the combination of a fixed current I_0 and a time-varying fluctuating component $\sigma_i(t)$, as illustrated in the diagram below.

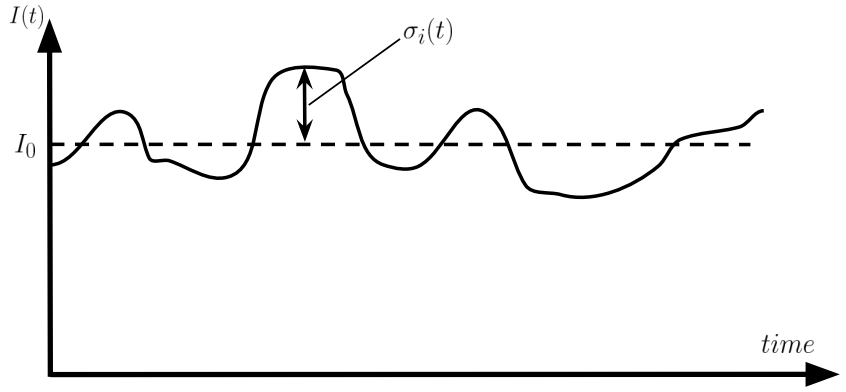

Figure 10: Intensity composed of the sum of two components.

The variable $\sigma_i(t)$ represents a random and time-dependent component that arises due to the inherent randomness of radiation events interacting within the detector.

The variance or mean square value is a statistical measure of the random component and is defined as the average of the square of the difference between the fluctuating current $I(t)$ and the average current I_0. This mean square value can be calculated using the following equation

$$\overline{\sigma_I^2(t)} = \frac{1}{T}\int_{t-T}^{t} \left[I(t') - I_0\right]^2 \, dt' = \frac{1}{T}\int_{t-T}^{t} \sigma_i^2(t') \, dt' \tag{4}$$

and the standard deviation follows as

$$\overline{\sigma_I(t)} = \sqrt{\overline{\sigma_I^2(t)}} \tag{5}$$

Based on Poisson statistics, it is important to remember that the standard deviation in the number of recorded events, n, during a specific observation period is typically expected to be

$$\sigma_n = \sqrt{n} \tag{6}$$

Hence, the standard deviation in the number of events happening at a rate r within a given effective measurement time T can be expressed as

$$\sigma_n = \sqrt{rT} \tag{7}$$

If all pulses contribute an equal amount of charge, the relative standard deviation in the measured signal resulting from random variations in the arrival times of the pulses can be calculated as

$$\frac{\overline{\sigma_I(t)}}{I_0} = \frac{\sigma_n}{n} = \frac{1}{\sqrt{rT}} \tag{8}$$

In this equation, $\overline{\sigma_I(t)}$ represents the average of the standard deviation in the measured current over time, T is the response time of the ammeter, and I_0 is the average current displayed on the meter. This relationship is valuable for assessing the uncertainty associated with a current mode measurement.

It is important to recognize that equation (8) assumes a constant charge (Q) produced in each event. Consequently, the equation accounts for random fluctuations in pulse arrival time but not for variations in pulse amplitude. Nevertheless, in many applications, the impact of these amplitude fluctuations on the overall variance of the signal is minimal, allowing the general findings of the equation to remain valid.

3.2.2 Pulse mode

When examining different uses of radiation detectors, we observe that current mode operation is employed in situations where event rates are exceedingly high. Additionally, detectors utilized for radiation dosimetry typically operate in current mode. On the other hand, MSV mode proves valuable in amplifying the response to events with significant amplitudes, making it commonly applied in reactor instrumentation. Nevertheless, for most applications, it is more advantageous to retain information regarding the amplitude and timing of individual events, which can only be achieved through pulse mode operation.

The characteristics of the signal pulse generated by a single event rely on the input properties of the circuit to which the detector is connected, typically a preamplifier. This circuit can be commonly depicted as illustrated below.

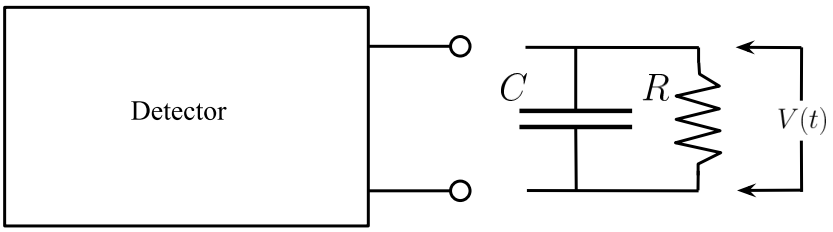

Figure 11: Detector connected in parallel with resistor and capacitor.

In the given context, R represents the input resistance of the circuit, while C represents the combined capacitance of the detector and the measuring circuit. For instance, if a preamplifier is connected to the detector, R corresponds to its input resistance, and C represents the total capacitance of the detector, the connecting cable, and the input capacitance of the preamplifier. The voltage $V(t)$ across the load resistance, which varies with time, serves as the fundamental signal voltage for pulse mode operation. There are two distinct operational extremes determined by the relative value of the time constant of the measuring circuit, which is calculated as the product of R and C, denoted as $\tau = RC$, according to basic circuit analysis.

3.2.2.1 Case 1. Small RC ($\tau \gg t_c$)

In this scenario, the external circuit is designed with a small time constant compared to the charge collection time. As a result, the current passing through the load

resistance R closely resembles the instantaneous current in the detector. The corresponding signal voltage $V(t)$, generated under these circumstances, exhibits a waveform that closely resembles the temporal behavior of the current produced within the detector, as depicted in figure 12.b. Radiation detectors are occasionally operated in such conditions when prioritizing high event rates or precise timing information over accurate energy measurements.

3.2.2.2 Case 2. Small RC ($\tau \ll t_c$)

The more prevalent approach is to operate detectors in the opposite extreme, where the time constant of the external circuit greatly exceeds the charge collection time of the detector. In this situation, minimal current flows through the load resistance during the charge collection period, and the detector current is temporarily accumulated on the capacitance. Assuming that the time gap between pulses is significant, the capacitance subsequently discharges through the resistance, causing the voltage across the load resistance to return to zero. This pattern of the signal voltage $V(t)$ is depicted in figure 12.c.

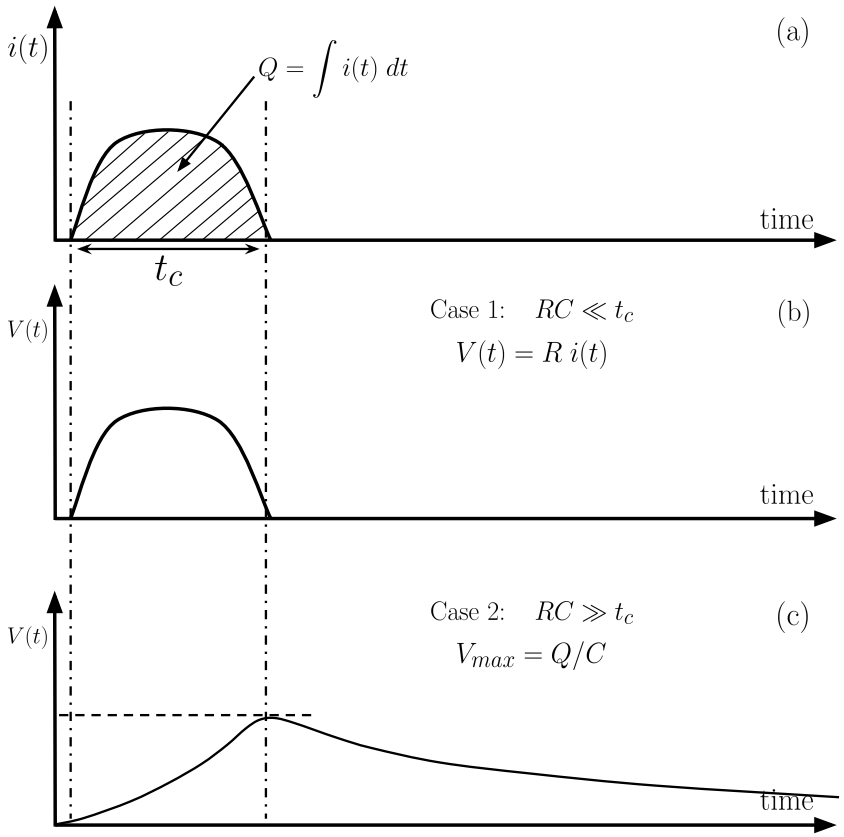

Figure 12: (a) The assumed current output from a hypothetical detector. (b) The signal voltage $V(t)$ for the case of a small time constant load circuit. (c) The signal voltage $V(t)$ for the case of a large time constant load circuit.

In the case of pulse-type operation of detectors, the more common scenario is when the time constant of the load circuit is much larger than the detector's charge collection time. It is important to draw some general conclusions from this. Firstly, the time it takes for the signal pulse to reach its maximum value is solely determined by the

charge collection time within the detector itself. The external or load circuit properties do not influence the rise time of the pulses. However, the decay time of the pulses, or the time it takes for the signal voltage to return to zero, is determined only by the time constant of the load circuit. This means that the leading edge of the pulse depends on the detector, while the trailing edge depends on the circuit. This generalization holds true for a wide range of radiation detectors operating under the condition where $RC \gg t_c$.

Secondly, the amplitude of the signal pulse, represented as V_{max} in figure 12.c, is simply determined by the ratio of the total charge Q generated within the detector during a radiation interaction to the capacitance C of the load circuit. Since the capacitance is typically fixed, the amplitude of the signal pulse is directly proportional to the charge produced within the detector. This relationship can be expressed by the simple equation

$$V_{max} = Q/C \tag{9}$$

Therefore, when a detector operates in pulse mode, it produces a series of individual signal pulses, each representing the outcome of a single interaction between a radiation quantum and the detector. By measuring the rate at which these pulses occur, we can determine the rate of radiation interactions within the detector. Additionally, the amplitude of each pulse indicates the amount of charge generated during each interaction. It is common to analyze the distribution of these pulse amplitudes, as it can provide insights into the incident radiation. For example, if the charge Q is directly proportional to the energy of the radiation quantum, the recorded distribution of pulse amplitudes will reflect the corresponding energy distribution of the incident radiation.

According to Equation (9), the relationship between V_{max} and Q is valid only if the capacitance C remains constant. In most detectors, the capacitance is determined by the physical characteristics of the detector, and it remains constant under normal operating conditions. However, in certain types of detectors, such as semiconductor diode detectors, the capacitance may vary with changes in operating parameters. In such cases, events with the same charge Q may result in voltage pulses of different amplitudes. To preserve the essential information provided by the magnitude of Q, a preamplifier circuit called a charge-sensitive configuration is commonly used. This circuit employs feedback to minimize the impact of capacitance variations and restore the proportionality between the output amplitude and the charge Q, even when C may change. While the simple RC representation shown at the beginning of this section is no longer accurate for this preamplifier configuration, the principle of collecting the current pulse across a capacitance and discharging it through a resistance remains valid.

Pulse mode operation is a preferred choice for most radiation detector applications due to several inherent advantages over current mode. Firstly, pulse mode offers higher sensitivity, often by several orders of magnitude, as each individual radiation quantum is detected as a distinct pulse. This allows for lower limits of detectability determined by background radiation levels. In contrast, current mode may require a much higher average interaction rate in the detector to achieve the same level of detectability.

The second and more significant advantage of pulse mode is that each pulse carries valuable information, which is often essential for specific applications. In both current

and MSV mode, this information on individual pulse amplitudes is lost, as all interactions, regardless of their amplitudes, contribute to the average measured current. Pulse mode preserves the amplitude information of each pulse, allowing for analysis and utilization of this data in various applications.

Due to these inherent advantages, the field of nuclear instrumentation heavily focuses on pulse circuits and pulse-processing techniques.

3.3 Background in Neutron Detectors

The natural background radiation contains neutrons, and any neutron detector will exhibit some level of response to these neutrons. For instance, a large-volume ^{3}He tube can easily register several counts per minute from the typical background radiation. The origins of these neutrons can be attributed to various sources, including those produced in the upper atmosphere through spallation reactions primarily caused by high-energy cosmic particles, such as protons. Additionally, secondary neutrons can be generated later in a cascade process either in the lower atmosphere or in the vicinity of the measurement location. The energy spectrum of these neutrons typically encompasses both slow and fast neutrons, with the highest energies extending into the hundreds of MeV range. Figure 13 illustrates a graph of measured background neutron spectra, which includes measurements taken at sea level and at various high altitudes. The spectrum observed at sea level demonstrates an increase in the slow neutron component, which arises from the thermalization of higher energy neutrons within the Earth and other nearby materials.

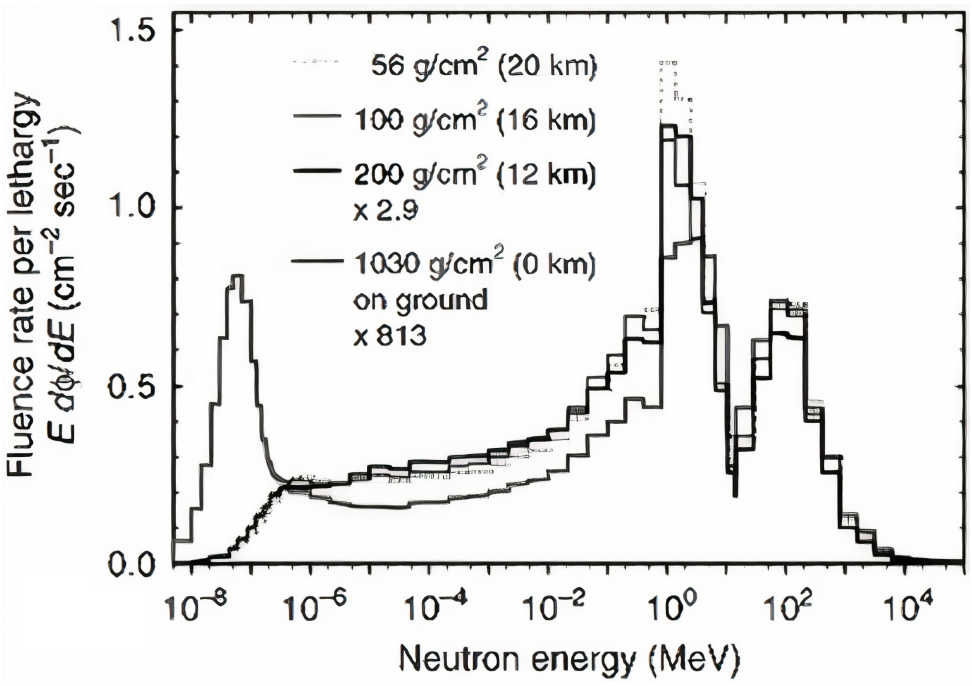

Figure 13: Measured energy spectra of back ground neutrons at ground level and several high altitudes. These spectra typically show peaks at several MeV and around 100 MeV. The ground level spectrum includes a peak at the left from thermalized neutrons.[30]

The absolute level of background neutrons at sea level shows significant variations across different locations worldwide. These variations are primarily influenced by the

magnetic shielding effect of the Earth, which causes fluctuations in the flux of energetic protons in the atmosphere based on the geomagnetic latitude. The neutron flux also depends on the specific materials present in the vicinity of the measurement site. The estimated flux values for neutrons at sea level range from around 30 to several hundred neutrons per square meter per second, depending on the global location and the characteristics of the nearby materials. One study [15] suggests a typical value of approximately 120 neutrons per square meter per second for ground-level measurements near sea level in the United States, while mountainous regions at high altitudes can exhibit values 10 to 20 times higher [28].

The impact of nearby materials on neutron measurements is often referred to as the "ship effect," which originated from early observations made when neutron monitors were brought aboard ships. It was widely noted that the measured neutron rate significantly increased compared to measurements taken over adjacent water. This increase in neutron background can be attributed to the local production of secondary neutrons in the massive steel structures of the ships. While some of these local neutrons may result from interactions with cosmic-ray muons, the majority appear to be generated by fast neutrons through additional spallation, knock-on, and other nuclear processes. This enhancement is not limited to steel but is also observed near other heavy materials such as lead. The magnitude of this effect seems to be directly proportional to the concentration of neutrons in the nuclei of the nearby material.[14]

3.4 Detectors based on fast neutron-induced reactions

Its is needed to detect not only if a neutron is passing by, but also its energy. This means that we can not rely on the slowing down of a fast neutron in a moderating material before its detection as a thermal neutron. The moderating process eliminates all information on the original energy of the fast neutron and normally cannot be used if an attempt is made to extract energy information. Moreover, the detection process is usually slow, as the neutron needs to undergo multiple collisions with moderator nuclei before the detection signal is generated, which can take a significant amount of time (that may take tens or hundreds of microseconds).

To overcome these limitations, it is possible to make the fast neutron directly induce a suitable nuclear reaction without the moderation step. This would allow the reaction products to have a total kinetic energy given by the sum of the incoming neutron kinetic energy and the Q-value of the reaction. By measuring the reaction product energies, the neutron energy can be determined by simple subtraction of the Q-value. Additionally, the detection process can potentially be fast, as the incoming fast neutron typically spends only a few nanoseconds in the active volume of the detector, and a single reaction can provide a detector signal.

However, the cross sections for typical fast-neutron-induced reactions are orders of magnitude lower than the corresponding thermal neutron cross sections. Thus, detectors based on this method will inevitably show a much lower detection efficiency than their thermal neutron counterparts.[14]

3.5 Types of detectors

3.5.1 Ionisation process

When ionizing radiation interacts with air or any other matter, it creates ions by releasing an orbital electron from a neutral air molecule, see figure 14.

The resulting ion pair includes a negatively charged electron and a positively charged molecule. This process occurs regularly due to radiation from natural and cosmic sources. Typically, the positively charged ion will recombine with a free electron, and the previously liberated electron will recombine with another positively charged ion.

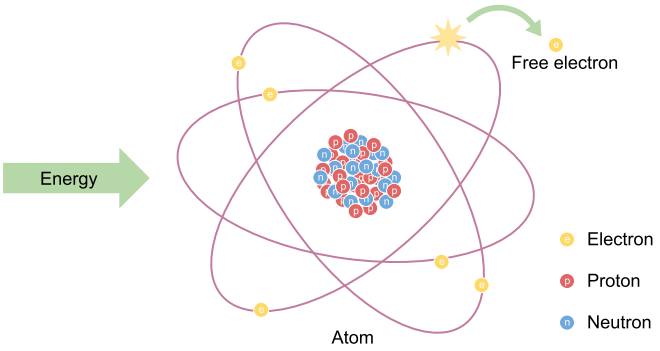

Figure 14: Ionization diagram.

When ionizing radiation interacts with air or any other matter, it creates ions by releasing an orbital electron from a neutral air molecule, see figure 14. The resulting ion pair includes a negatively charged electron and a positively charged molecule. This process occurs regularly due to radiation from natural and cosmic sources. Typically, the positively charged ion will recombine with a free electron, and the previously liberated electron will recombine with another positively charged ion.

The roentgen (R) is the basic unit of measurement for gamma and x-ray radiation exposure, and it indicates the degree of ionization in dry air. Specifically, one R is equal to the creation of 2.082×10^9 ion pairs in 1 cubic centimeter of dry air at standard temperature and pressure. In terms of exposure rate, a radiation field of one R per hour generates 2.082×10^9 ion pairs every hour. The number of ion pairs generated is also proportional to the energy of the original photon.

When a voltage is applied to two electrodes within a chamber filled with gas, the ion pairs components are drawn towards the electrode with the opposite charge. The negatively charged electrons, or negative ions, are attracted to the positive electrode, or anode, while the positively charged ions, or remaining molecules, are drawn towards the negative electrode, or cathode. However, because the positive ion is significantly more massive than the negative ion, its movement is restricted and can be disregarded. An electrical current is then generated by the movement of electrons to the anode. This instrument is an ionisation chamber.

3.5.2 Ionisation chamber

An ionization chamber uses an electrically conductive container as the cathode to isolate a gas volume. The chamber includes an electrically insulated anode electrode at its center. Applying a low voltage to the chamber creates an electric field, initiating ion flow and generating an electrical current. Gradually increasing the voltage will eventually cause every negative ion to be attracted to and collected by the anode, which is referred to as the saturation level or Griger-Mueller region. The saturation voltage

required may vary for different radiation levels. The key is to maintain a voltage high enough to achieve saturation but low enough to avoid the proportional region. Figure 15 is a schematic diagram showing the primary components of a basic ion chamber.

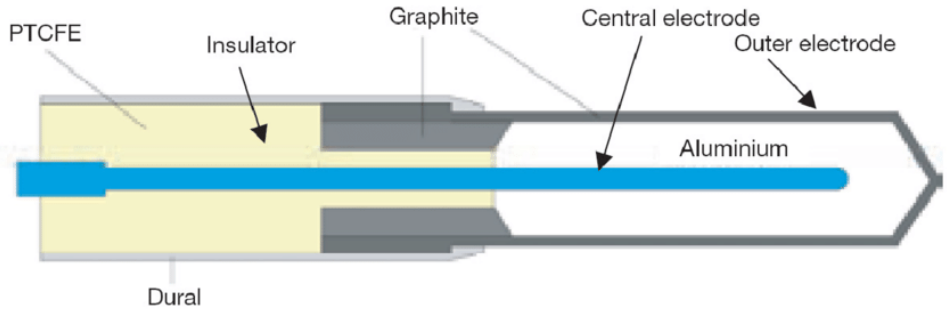

Figure 15: Schematic of a cylindrical ionisation chamber. [22]

The different regimes in which the ionisation chambers can operate depending on the value of the voltage applied to them are shown in the figure 16.

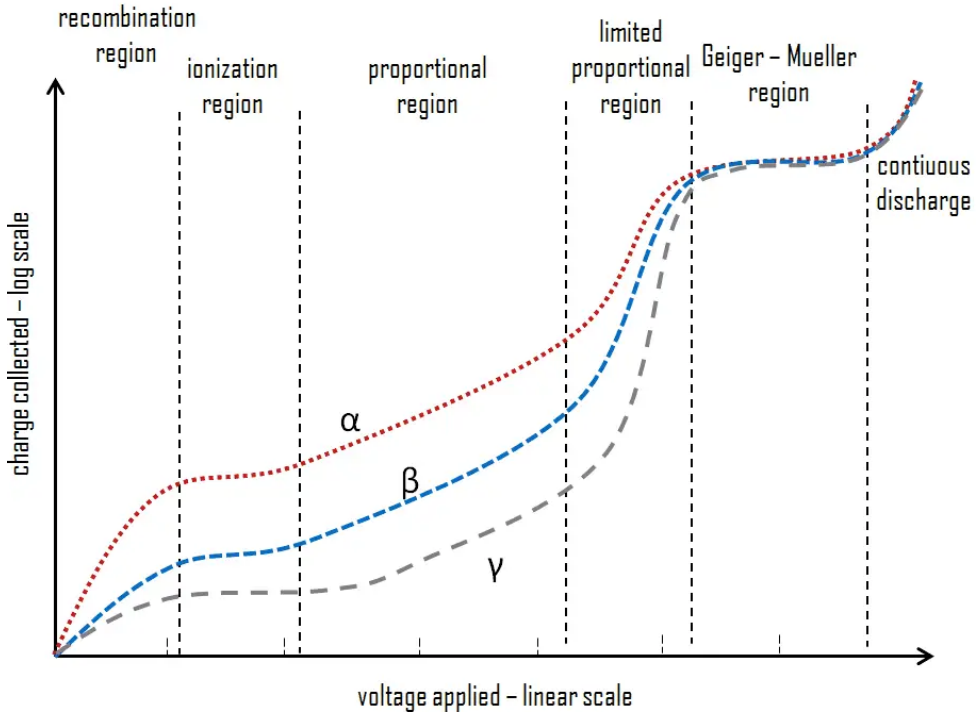

Figure 16: Regions of gaseous ionization detectors.
`https://www.radiation-dosimetry.org/wp-content/uploads/2019/12/Gaseous-Ionization-Detectors-Regions-min.png`

Note that saturation voltage in an ionization chamber is unrelated to saturation in a G-M detector, and the use of the same term is coincidental.

The flow of electricity, measured in amperes, indicates the number of electrons that move past a specific point in an electrical circuit within a certain amount of time. One ampere corresponds to 6.281×10^{18} electrons passes through a point on a circuit in 1 second. 2.082×10^{9} electrons generated in 1 cm^3 of dry air would generates a current of only 9.208×10^{-14} amperes for every cubic centimeter of chamber volume. In

a typical hand-held ion chamber with a detector volume of approximately 300 cubic centimeters, the current flow would be 27.62×10^{-12} amperes. This level of current is extremely small and challenging to measure precisely. Hence, ion chambers are not generally utilized to measure low levels of radiation. To overcome this obstacle, the gas in the chamber volume can be pressurized to increase its density and create more interactions with the incoming radiation, resulting in a larger current for a specific amount of photons. [13]

3.5.2.1 The Ionization Current

In the presence of an electric field, the drift of the positive and negative charges represented by the ions and electrons constitutes an electric current. If a certain amount of gas is continuously exposed to radiation, the rate at which ion pairs are formed remains constant. For any small test volume of the gas, this rate of formation will be exactly balanced by the rate at which ion pairs are lost from the volume, either through recombination or by diffusion or migration from the volume. Assuming recombination is insignificant and all charges are efficiently collected, the resulting steady-state current becomes a precise indicator of the ion pair formation rate within the tested volume. Measurement of this ionization current is the basic principle of the de ion chamber.

The diagram presented in figure 17 demonstrates the fundamental components of a simple ion chamber. A certain amount of gas is contained within an area where an electric field can be generated by applying an external voltage.At equilibrium, the current flowing in the external circuit will be equal to the ionization current collected at the electrodes, and a sensitive ammeter placed in the external circuit can therefore measure the ionization current.

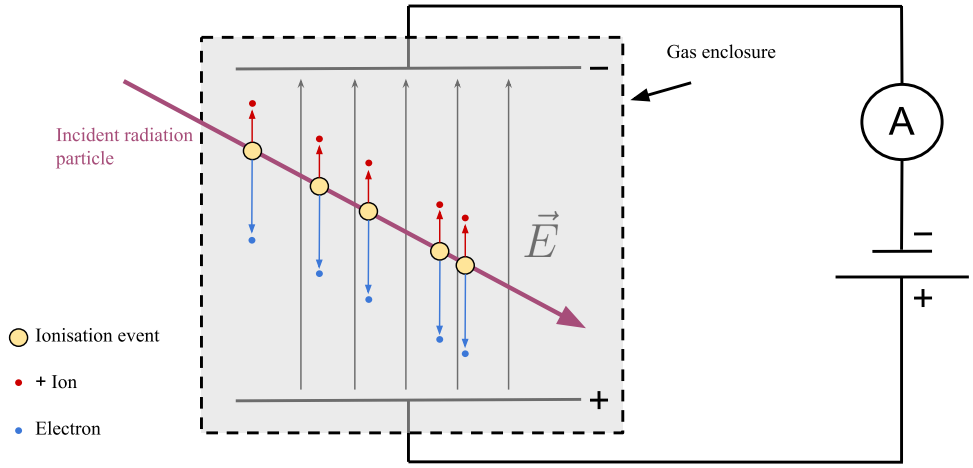

Figure 17: Schematic of how ionizing radiation generates charge pairs.

The current-voltage characteristics of such a chamber are depicted in figure 18. Disregarding certain subtle effects associated with variations in diffusion properties between ions and electrons, in the absence of an applied voltage, no net current should flow because no electric field exists within the gas. Ions and electrons that are generated ultimately vanish through recombination or diffusion from the active area. As

the voltage increases, the resulting electric field begins to separate the ion pairs more rapidly, leading to a decrease in recombination. The positive and negative charges are also propelled towards their respective electrodes, reducing the equilibrium concentration of ions in the gas. This further suppresses volume recombination between the point of origin and the collecting electrodes. Consequently, the measured current rises with the applied voltage as these effects minimize the loss of the original charge. At a sufficiently high voltage, the electric field becomes strong enough to effectively suppress recombination to a negligible level, allowing all the initial charges created through ionization to contribute to the ion current. Further increasing the voltage does not result in a higher current since all charges are already collected, and their formation rate remains constant. This corresponds to the region of ion saturation, in which ion chambers are typically operated. In these conditions, the current measured in the external circuit accurately reflects the rate at which all charges are formed due to ionization within the active volume of the chamber.

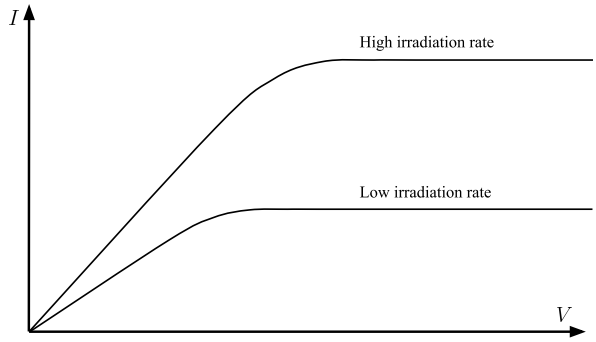

Figure 18: I-V behavior at low and high irradiance intensities.

Assuming recombination can be disregarded, it is important to highlight that the saturated current does not alter regardless of whether the ionization electrons remain unattached and drift as free electrons, or if they become attached to gas molecules and form negative ions. In the case of attachment, the drift velocity becomes significantly slower, but the equilibrium concentration of negative charges increases by the same factor. Since the current is determined by the product of charge density and drift velocity [14], the resulting current remains unchanged, as if the electrons were drifting freely.

3.5.3 Fission chambers

A fission chamber is a type of nuclear radiation detector that uses nuclear fission to detect the presence of neutrons in a radioactive environment. It consists of a small cell with stainless steel walls and electrodes, which is filled with a noble gas, such as argon, at elevated pressure. The chamber walls are usually coated with highly enriched uranium to increase the ionisation current produced by the neutrons interacting with the material. When a neutron enters the chamber, it interacts with the nucleus of a uranium atom, causing it to split into fission fragments that are able to ionise the gas. The resulting electric current can be measured and is used to detect the presence of neutrons and measure their flux and energy. Fission chambers are common in nuclear reactor monitoring and radiation measurements in high-energy environments.

Fission chambers can be customized for use within a hight neutron flux, regardless of the power levels that may be encountered during their use. To increase the ionization current, the walls of the chamber are often lined with highly enriched uranium. These miniaturized ion chambers are typically constructed with stainless steel walls and electrodes, and their operating voltage ranges from 50 to 300 V. Argon gas is a common choice for filling the chamber and is used at a pressure of several atmospheres. The increased pressure helps to ensure that the fission fragments produced within the gas do not travel beyond the small dimensions of the detector.

The depletion or "burn up" of neutron-sensitive material is a significant issue during prolonged use of this type of detectors. As an illustration, a fission chamber containing ^{235}U may experience a sensitivity reduction of around 50% after being exposed to a neutron fluence of about 1.7×10^{21} n/ cm^2. One approach to mitigating the effects of burn up in fission chambers is to incorporate fertile and fissile material in the neutron-sensitive lining of the chamber. Regenerative chambers that use this technique gradually convert the fertile isotopes to fissile nuclei, which helps to offset the burn up of the original fissile material present in the lining. By using this method, the long-term response of fission chambers can be significantly enhanced. For example, it has been reported that fission chambers containing a blend of ^{238}U and ^{239}Pu can maintain a sensitivity that does not fluctuate by more than $\pm$5% over a neutron fluence of 4.8×10^{21} n/cm^2. Comparable outcomes have also been attained with fission chambers containing a mixture of ^{234}U and ^{235}U.

Fission ion chambers that have been operated for long periods in high neutron fluxes demonstrate a residual current or memory effect caused by the accumulation of fission products within the chamber. These fission products emit beta and gamma rays that ionize the fill gas of the chamber and create a substantial ion current. Figure 19 illustrates the expected outcomes when the current from a fission chamber is monitored after it has been removed from long-term exposure to a steady-state neutron flux. The residual current I is depicted as a proportion of the steady-state current I_0 observed during the neutron irradiation. Approximately 0.1% of the signal current persists one minute after removal, while after ten days, the decay of the fission product activity is sufficient to reduce the residual current to around 10^{-5} of the steady-state signal.

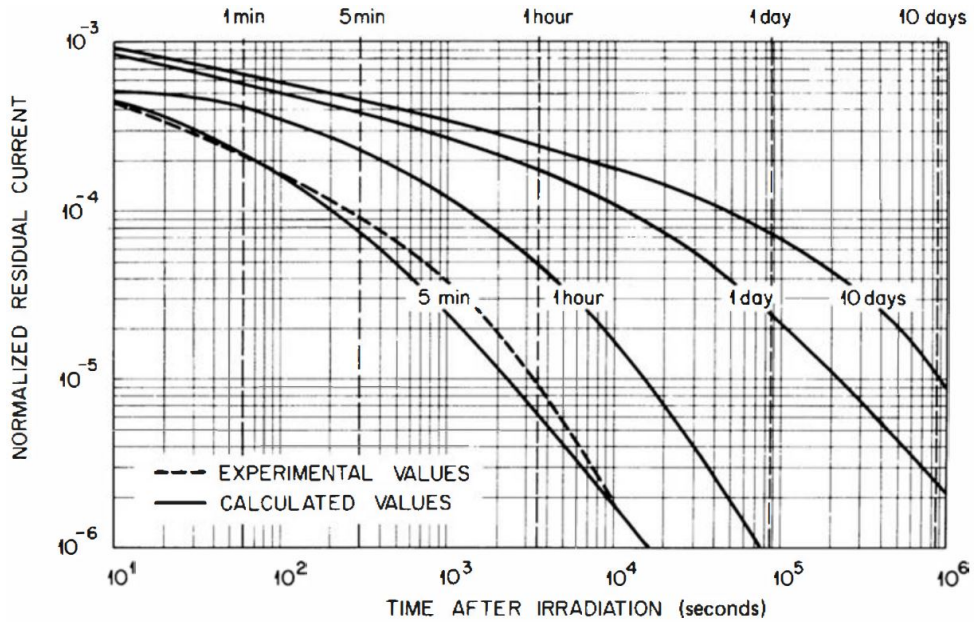

Figure 19: Memory effect in fission chambers corresponding to various steadystate irradiation times. [14]

Figure 20 demonstrates an effect that can be significant in ion chambers designed to cover a wide range of irradiation rates. At lower rates, the region of ion saturation is achieved at a lower voltage than at higher rates. At higher currents, the density of ionization is correspondingly greater, and recombination occurs more readily than at lower currents. As a result, the electric field needed to prevent recombination is higher at high rates, as indicated by the increased voltage required to attain ion saturation. It is crucial to choose an operating voltage for these chambers at the highest irradiation rate or the largest current that may be encountered.

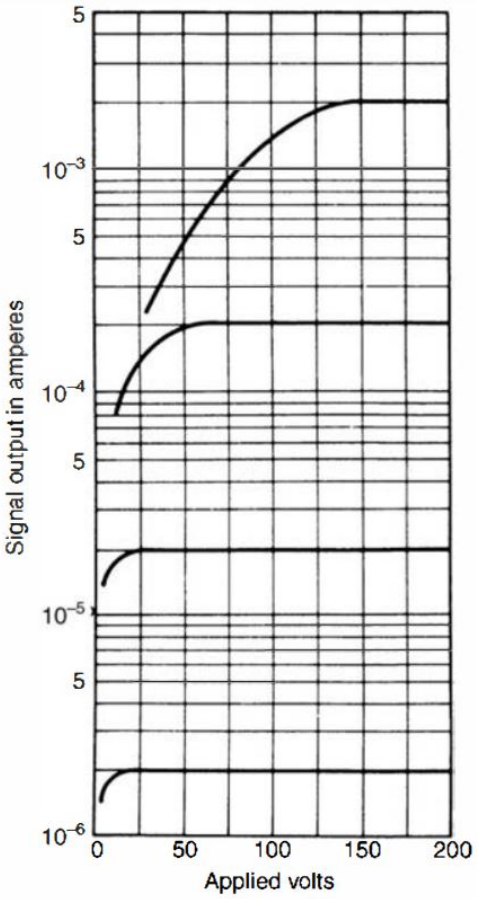

Figure 20: Typical current-voltage characteristics of a fission chamber at different neutron irradiation levels. [14]

3.5.4 Self powered neutron detectors. SPND

Not being the main object of this work, it has been considered pertinent to formally present the self powered neutron detectors at the request of IFMIF-DONES due to the fact they have detectors of this type that will be used in future experiments at the UGR facilities.

A specific type of neutron detector commonly used for in-core applications is known as a self-powered detector. These detectors utilize a material that has a relatively high neutron capture cross-section, resulting in subsequent beta or gamma decay. The basic principle of operation for this type of detector involves directly measuring the current produced by beta decay after neutron capture. This current is expected to be proportional to the rate at which neutrons are captured within the detector. The unique aspect of self-powered detectors is that they do not require an external bias voltage since the beta decay current is measured directly. This is why they are referred to as self-powered detectors. Another variation of the self-powered detector takes advantage of the gamma rays emitted following neutron capture. A portion of these gamma rays will interact within the detector, generating secondary electrons through various mechanisms such as Compton scattering, photoelectric effect, and pair production. The current produced by these secondary electrons can then serve as the primary signal for detection.

The self-powered detector is referred to by several alternative names. In honor of the pioneering contributions made by J.W. Hilbom, it is occasionally known as Hilborn detectors. Other names encountered in literature include beta emission detectors, collectrons, electron emission detectors, and PENA (primary emission, neutron activation) detectors. Nevertheless, the term self-powered neutron detector (SPND) is the most widely used to describe this group of devices.

Self-powered detectors offer several advantages over other neutron sensors, including their compact size, cost-effectiveness, and the simplicity of the associated electronics. However, there are certain drawbacks associated with these detectors. One limitation is the low level of output current they generate, making them less sensitive to changes in the neutron energy spectrum. Additionally, many types of self-powered detectors have a relatively slow response time. Due to the nature of the signal, which typically consists of a single electron resulting from a neutron interaction, operating in pulse mode is impractical. As a result, self-powered detectors are always operated in current mode.

3.5.4.1 Self-powered detectors based on beta decay

Figure 21 depicts a schematic of a typical self-powered neutron (SPN) detector based on beta decay.

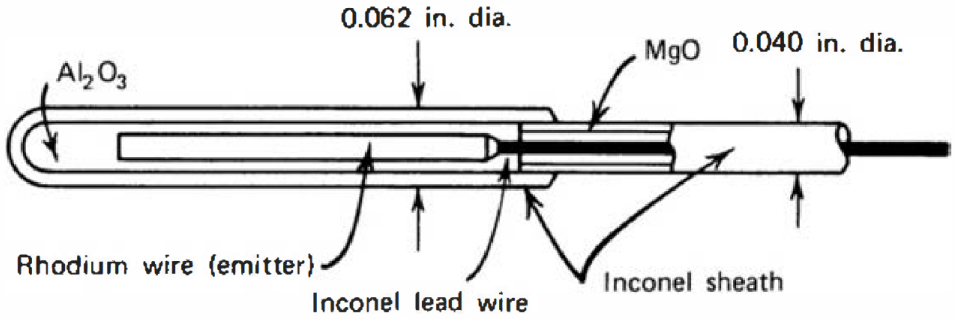

Figure 21: Cross-sectional view of a specific self-powered detector design. [27]

The key component of this detector is the emitter, which consists of a material selected for its relatively high neutron capture cross section, resulting in the production of a beta-active radioisotope. It is desirable for the remaining parts of the detector to have minimal interaction with neutrons, so construction materials with low neutron cross sections are chosen. Figure 22 presents several possible sequences that can contribute to the measured current.

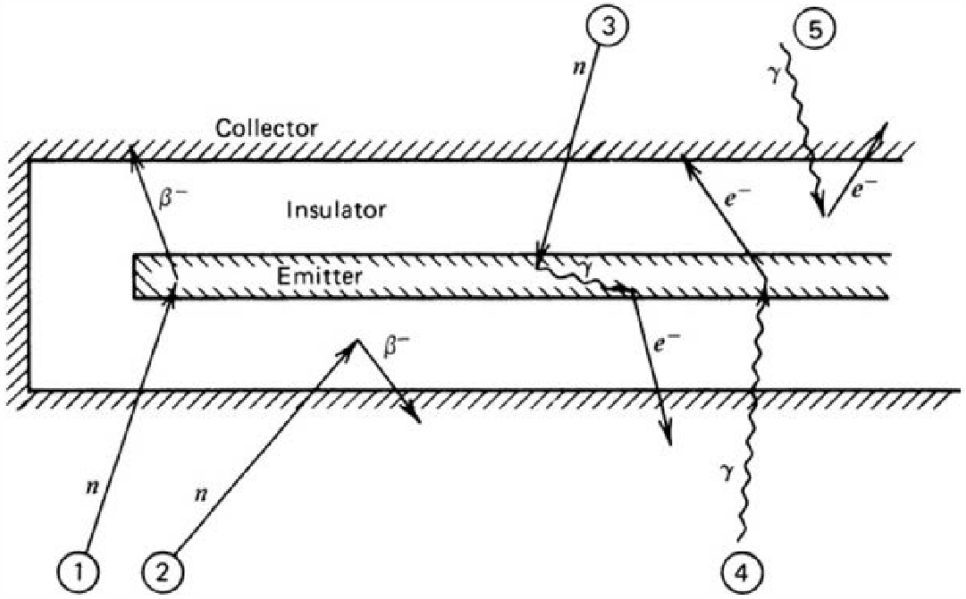

Figure 22: Representative events that can take place in an SPN detector. Events 1 and 2 are neutron capture followed by β-decay. Event 3 shows the interaction of a prompt gamma ray emitted upon neutron capture, giving rise to a fast secondary electron. Events 4 and 5 show interfering fast electrons arising from interactions of external gamma rays. In standard SPN detectors, event 1 is the basis of its neutron response. In those with fast response, event 3 is the preferred mode of interaction. [14]

The operational principles are straightforward: The current, primarily composed of beta rays emitted by the emitter, is measured between the emitter and an outer shell known as the collector. An insulator fills the space between them, which must be carefully selected to withstand the extreme temperature and radiation conditions typically encountered in a reactor core (for its commond use). Metallic oxides, such as magnesium or aluminum oxide, are commonly used as insulators, while the collector is typically made of high-purity stainless steel or Inconel. During the fabrication of these detectors, meticulous care is taken to maintain cleanliness, as any contamination by substances that could become radioactive would introduce interfering currents to the

measured signal. The small dimensions shown in figure 21 are necessary due to the limited available clearances for instrument channels within typical reactor cores.

The performance of the detector greatly depends on the selection of the emitter material. When choosing the emitter, several factors come into play, including the neutron capture cross section, energy, and half-life of the resulting beta activity. It is crucial to strike a balance in the neutron capture cross section—neither too high nor too low. Very low cross sections would yield detectors with low sensitivity, while excessively high cross sections would lead to rapid depletion of the emitter material due to the intense neutron fluxes found in reactor cores (once again, its common use). The beta rays produced by the emitter should have sufficiently high energy to prevent excessive self-absorption within the emitter or insulator. Additionally, the half-life of the induced activity should be as short as possible, enabling the detector to promptly respond to rapid changes in neutron flux.

Taking into consideration these considerations, rhodium and vanadium have emerged as the two most popular choices for emitter materials. Table 1 provides a summary of the key properties of these materials when utilized as emitters in self-powered detectors.

Emitter material	**Nucleide of interest and percent abundance**	**Activation cross section at thermal energy**	**Half-life of induced beta activity**	**Beta endpoint energy**	**Typical neutron sensitivity**
Vanadium	$^{51}_{23}$V(99.750%)	4.9 barns	225 s	2.47 MeV	$5 \times 10^{-23} \frac{\text{A}}{\text{n/cm}^2 \cdot \text{s}}$
Rhodium	$^{103}_{45}$Rh(100%)	139 barns	44 s	2.44 MeV	$1 \times 10^{-21} \frac{\text{A}}{\text{n/cm}^2 \cdot \text{s}}$
		11 barns	265 s		

Table 1: Properties of emitter materials for SPN Detectors based on beta decay

Vanadium exhibits a relatively simple beta decay with a half-life of 225 seconds, whereas rhodium undergoes a more complex beta decay with a mixture of half-lives of 44 and 265 seconds. Figure 23 illustrates the response of these materials to a sudden change in neutron flux.

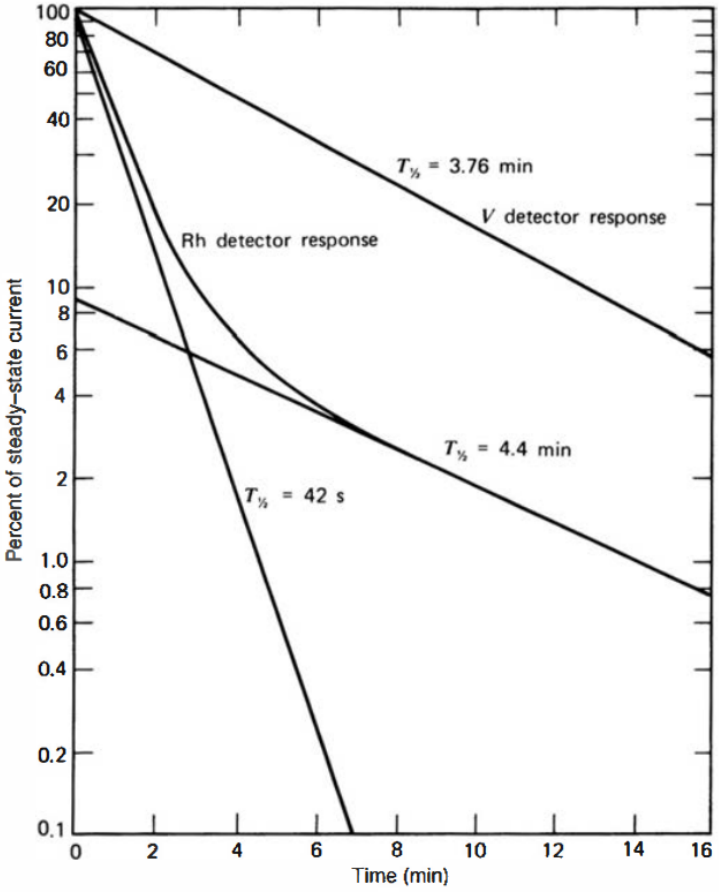

Figure 23: Response of rhodium and vanadium SPN detectors to an abrupt drop to zero of a steady-state neutron flux. [27]

Despite vanadium's lower sensitivity and somewhat slower response compared to rhodium, vanadium emitters have gained greater prominence in reactor applications. This is primarily due to their significantly reduced burnup rate, enabling their use over extended periods of several years in typical reactor flux conditions.[14]

In its simplest form, a self-powered detector that exhibits a single mode of induced activity and negligible burnup will exhibit the following behavior when subjected to a neutron flux over a duration of time t:

$$I(t) = C\, q\, \sigma\, N\, \phi\left(1 - e^{-\lambda t}\right) \tag{10}$$

Where:

- C = dimensionless constant reflecting the specific geometry and collection efficiency of the detector.
- q = charge liberated (number of beta particles x e) per neutron absorbed.
- σ = activation cross section of the emitter material.
- N = number of emitter atoms.
- ϕ = neutron flux.

- λ = decay constant of activity produced in the emitter.

When the detector has reached saturation, meaning it has been exposed to the neutron flux for a duration significantly longer than the half-life of the induced activity, the steady-state current is given simply by:

$$I_{sat} = C\ q\ \sigma\ N\ \phi \tag{11}$$

The saturated current is proportional to the neutron flux and consequently can serve as a corresponding monitor of the neutron flux level.

A more comprehensive analysis of the detector output requires consideration of various additional factors. These include the reduction in neutron flux due to emitter self-shielding, the presence of Compton and photoelectrons resulting from accompanying gamma rays during the beta decay process, and the likelihood of beta particles being absorbed within the emitter material. Some electrons may be halted in the insulator before reaching the collector, while others may be generated within the insulator and travel towards either the emitter or the collector. Over time, an equilibrium is established where the net charge flowing into the insulator is balanced by the charge flowing out. Extensive Monte Carlo simulations have demonstrated that the current arising from processes occurring within the insulator typically accounts for less than 15% [31] of the total current, thus not significantly influencing the detector response. Detailed physical models have been developed [31] [17] to accurately predict [23] the response of self-powered neutron detectors, incorporating most of these effects.

3.5.4.2 Self-powered detectors based on secondary electrons from gamma decay

One of the main drawbacks of self-powered detectors based on beta decay is their relatively sluggish response time. Efforts have been made to address this issue through the application of electronic or digital signal processing techniques,[25] [1]. However, it would be more desirable to enhance the inherent response time of the detector itself. One method to achieve this goal is to rely on the generation of secondary electrons produced by capture gamma rays that swiftly follow neutron capture in the emitter (as illustrated in figure 22). These capture gamma rays are typically emitted within a very short duration, in contrast to the slower decay of typical neutron-induced beta activities. Even in vanadium and rhodium detectors, there exists a component of the signal that corresponds to the emission of capture gamma rays immediately after neutron capture in these materials. Although this component is much smaller compared to the signal from the beta current, it contributes to the overall response. The reported ratio of this component to the delayed signal in commercial vanadium detectors is approximately 6.5% [25].

When aiming for fast self-powered detectors, the focus is often on selecting a specific emitter material that optimizes the signal generated by the rapid capture of gamma rays. Cobalt has been extensively studied and used as an emitter with fast response times,[2] [3] [16] and commercially available detectors also make use of cadmium. The performance and sensitivity of alternative emitter materials have been investigated,[19] [29] although, in general, prompt detectors exhibit lower neutron sensitivity compared to those based on beta decay. Nevertheless, their ability to provide a much quicker response makes them suitable for certain applications where speed is crucial.

The impact of external gamma rays can also be significant for certain emitter materials. When gamma rays interact with the detector, they can generate secondary electrons, contributing to a detectable signal as shown in figure 22. This signal may be positive or negative, depending on the direction of current flow between the emitter and collector. The specific construction of the detector determines the prevailing polarity. Emitter materials commonly used in neutron-sensitive detectors, such as rhodium, vanadium, or cobalt, typically exhibit gamma-ray responses that are only a few percent of the neutron response.[26] Detectors utilizing zirconium emitters primarily respond to gamma rays, while other materials like platinum, osmium, or cerium produce a mixed response. Platinum detectors, which offer a combination of prompt and delayed response, have gained popularity and have been extensively analyzed.[18] [32] [33]

In all self-powered detectors, the influence of neutron and gamma-ray interactions in the signal cable can be significant. Therefore, careful consideration must be given to the choice of construction materials for the signal cable [21] that connects to the detector, particularly in areas exposed to high radiation fields. To minimize false signals caused by cable interactions, twin signal leads are often employed. One lead is connected to the emitter through the cable, while the other lead is included in the same cable but terminated without electrical contact in close proximity to the emitter. By electronically subtracting the signal from the unconnected lead from the detected current in the connected lead, the effects of cable interactions are effectively mitigated.

4 Methodology and materials

4.1 Metelodogy

In this master's thesis, an exhaustive analysis of the factory acceptance data has been carried out, without the need for additional experimental work. In addition, several protocols have been established to continue the analysis of the detectors in the future and a detailed theoretical development of the operating modes of these detectors has been carried out, formally presenting each one of them.

The analysis of the factory acceptance data has been performed using the Python programming language in Jupyter notebooks, as mentioned above. In addition, the measurement protocols to be carried out at the UGR once the X-ray generator is operational again have been established in these notebooks.

In the report, the operation of the detectors involved in this project has been developed, as well as their different operation modes. The most relevant data obtained from the analyses carried out in the Jupyter notebooks have also been included.

4.1.1 The microchambers data

The employees at PHOTONIS Nuclear Instrumentation were responsible for collecting the numerical data related to the ionization and fission microchambers. The initial step involved gathering all the necessary information from the documentation

provided by the sensor manufacturer. Subsequently, the numerical data from each sensor's datasheets were digitized to enable data processing in Python using a Jupyter Notebook.

The data were previously prepared by grouping them in a file extension ".xlsx" for a more organized data management. Due to the limited data provided, cleaning was not considered, and incomplete or inconsistent data were not analyzed. No normalization or transformation of the data was necessary.

The variables selected for study were all the data sets provided by the manufacturer as long as they were complete. These variables are the original ones, i.e., no derived variables were analyzed.

In order to analyze the data and explore potential relationships between them, all the data has been charged and processed using the Jupyter notebooks specifically created for this study.

All the detectors considered in this study had to undergo five tests to confirm their validity for use. These tests are as follows:

1. Test 1: I-V characteristic analysis. Each detector was subjected to a test where it was irradiated with X-rays at a constant intensity. The intensity of the X-rays passing through the detector was measured and recorded while the polarization voltage was varied.

2. Test 2: I-I characteristic analysis. Each detector was subjected to a test where it was irradiated with X-rays at variable intensity. The intensity of the X-rays passing through the detector was measured and recorded while the intensity of the incident X-rays was changed. The polarization voltage remained constant during this test.

3. Test 3: Coaxial cable analysis. The coaxial cable connected to the detector needed to be studied to understand its behavior. This test is performed on the cable alone, without the detector attached. Using a signal generator, a known signal is sent through the cable, and with the help of an oscilloscope, the signal at the output is analyzed. By noting the input and output signal amplitudes, the signal attenuation due to the cable can be determined.

4. Test 4: Impedance analysis. The coaxial cable connected to the detector forms a system that needs to be examined for any small cracks, bends, or faulty soldering that could affect the signal. To achieve this, a signal was sent to the cable-detector assembly, and the reflected signal was analyzed using an electrometer. The electrometer is capable of providing the impedance of the system based on the position relative to the electrometer.

5. Test 5: Leakage current analysis. Since the current recorded by the amperemeter is in the order of tens of nanoamperes, it is easily eclipsed by the leakage current that may occur in the system. It is therefore necessary to characterize this leakage current, both at ambient temperature and at 350°C.

These five tests were supposed to be conducted for each detector, but that has not been the case. Tests number 3 and 4 have not been performed for any detector. A future pending task will be to carry out these tests for all (except three) the detectors in the X-ray generator facilities of the UGR. Test number 2 has only been conducted for some detectors, not all of them. The detectors for which test number 2 was performed are as follows:

- Ionization Cameras (ID Cameras): 201, 202 and 204.
- Fission Cameras (ID Cameras): 210, 123, 124 and 207.

Regarding tests number 1 and 5, it has been conducted for all the detectors according to a protocol that the company responsible for the test has chosen not to share.

All five of these tests will be carried out at the UGR X-ray generator facilities in order to repeat them with a larger number of data taken. The set up that will be used at the UGR to reproduce these tests can be seen in images 24, 25, 26 and 27.

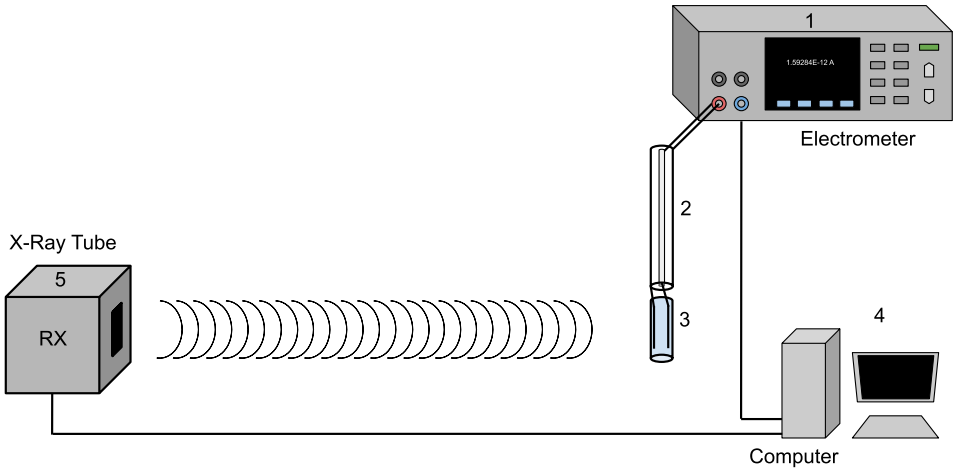

Figure 24: Scheme of the set up of test 1 and 2 to be carried out at the UGR facilities.

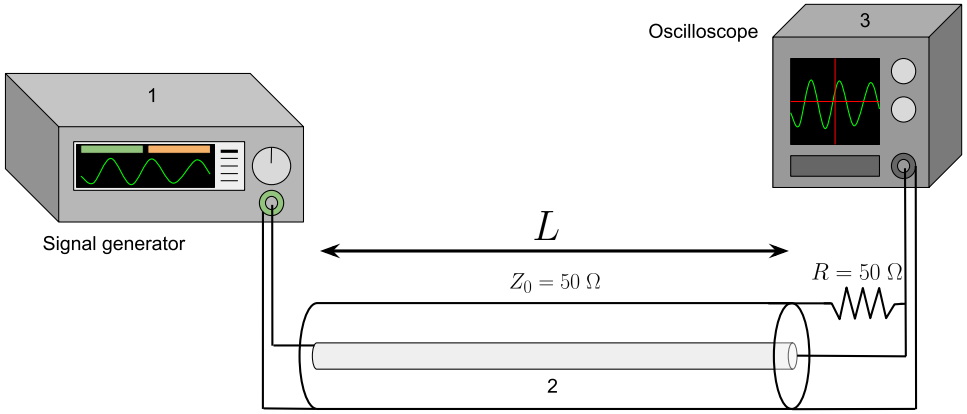

Figure 25: Scheme of the set up of test 3 to be carried out at the UGR facilities.

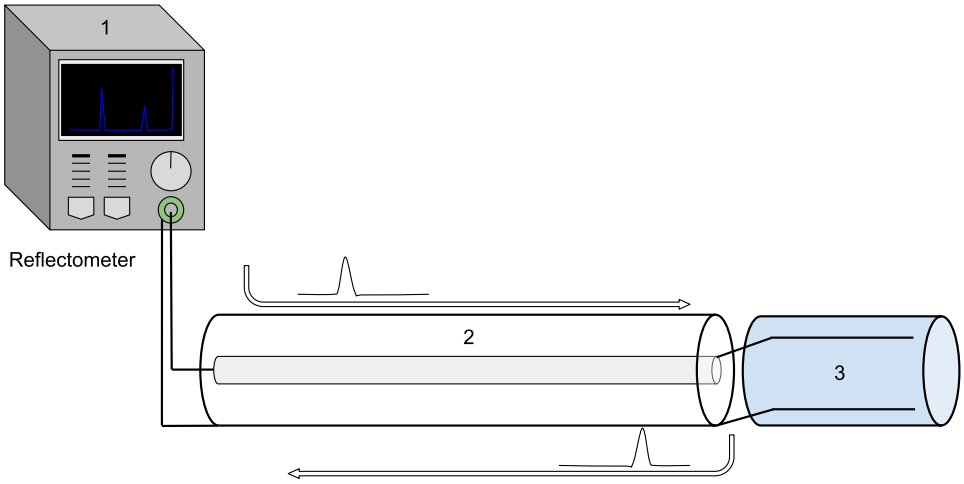

Figure 26: Scheme of the set up of test 4 to be carried out at the UGR facilities.

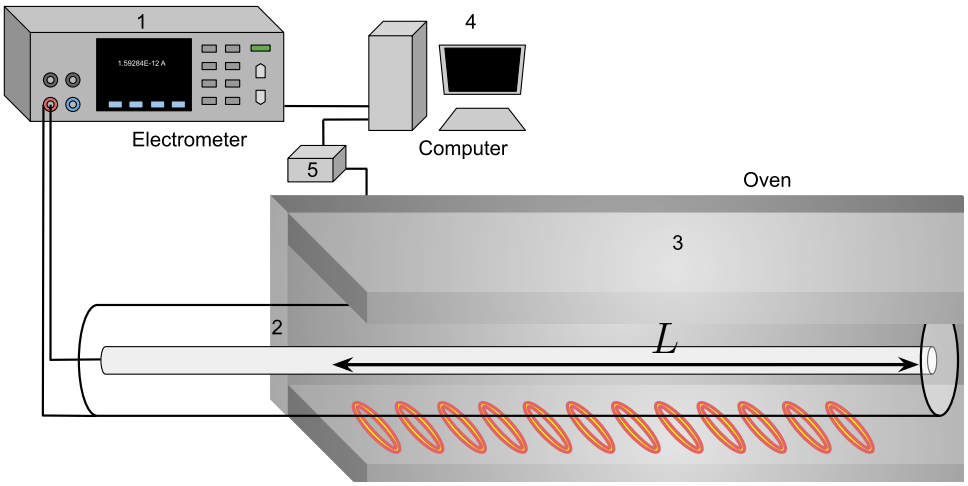

Figure 27: Scheme of the set up of test 5 to be carried out at the UGR facilities.

4.1.2 The bias voltage of the microchambers

The following criteria have been developed to determine the optimum bias voltage. The optimum bias voltage of each microchamber is ideally determined by the zero variation of the detected electric current intensity while the irradiance remains constant and the potential bias is varied.

The optimal bias voltage value will then be considered to be the one that makes the slope of the tangent curve to a polynomial of degree $\text{round}(\sqrt{N})$ *that best fits the data as close to zero as possible. Where N is the length of the data set.*

4.2 Materials

In this work, the data provided by the manufacturer have been used to validate the detectors. Although neither detectors nor radiation sources were used directly, the technical specifications of the instruments associated with the data used are presented below.

4.2.1 Radiation source

In this work, only the behaviour of the detectors has been studied within an X-ray beam which had a cross section of 1.5×1.5 mm^2. The beam was generated by an X-ray tube with the following characteristics:

- RX tube voltage 120 kV
- Anode current 9 mA
- Filtration 1mm Beryllium
- Detector source distance 65 mm

The X-ray generator model used by Photonis for its tests is the Philips X-Ray MG 165 with a 120 kV tube 28. It is manufactured by YXLON International GmbH, located at Essener Bogen 15, 22419.

Figure 28: Philips X-Ray MG 165 with a 120 kV tube.

4.2.2 Detectors

ICs and FCs characteristics (made by Photonis) are detailed in Table 2.

Characteristic	CRG10/C5B	CFUR43/C5BU5	CFUR43/C5BU8	CFUR44/C5BU8
Filling gaz	Argon	Argon	Argon	Ar + 4% N
Internal gaz pressure (bar)	5	5	5	15
Total uranium mass (μg)	0	300	300	300
Uranium isotopic composition	-	^{235}U >92%	^{238}U: 99.8% ^{235}U: 0.2%	^{238}U: 99.8% ^{235}U: 0.2%
Total activity (Bq)	0	951	12	12
Working mode	Curent mode	Current mode	Current mode	Pulse mode
Quantity	15	3	9	3

Table 2: Nuclear characteristics of the detectors

All these detectors have the same dimensions, which can be seen in the figure 29.

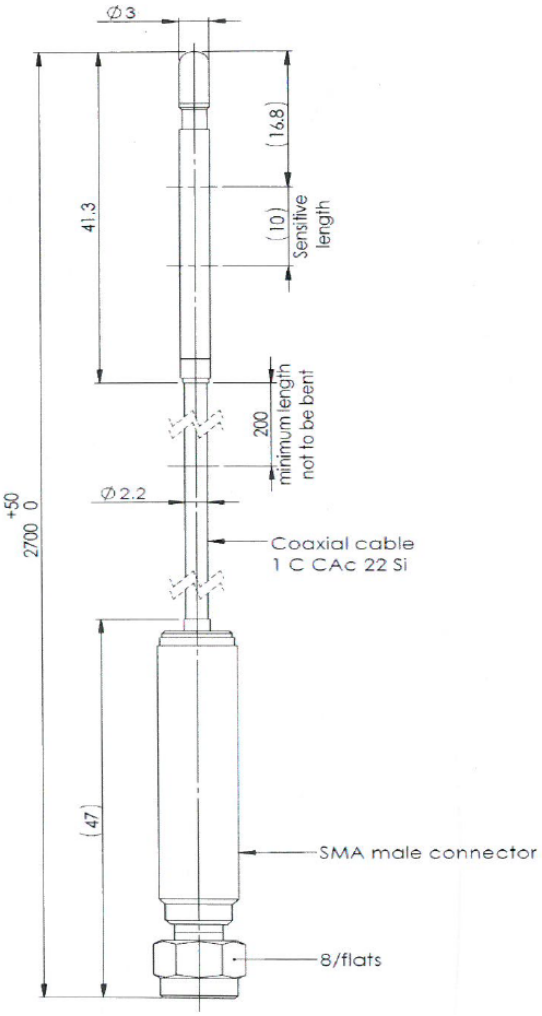

Figure 29: Dimension of all microchambers. All dimensions in mm. All dimensions in brackets are given on an indicative basis.

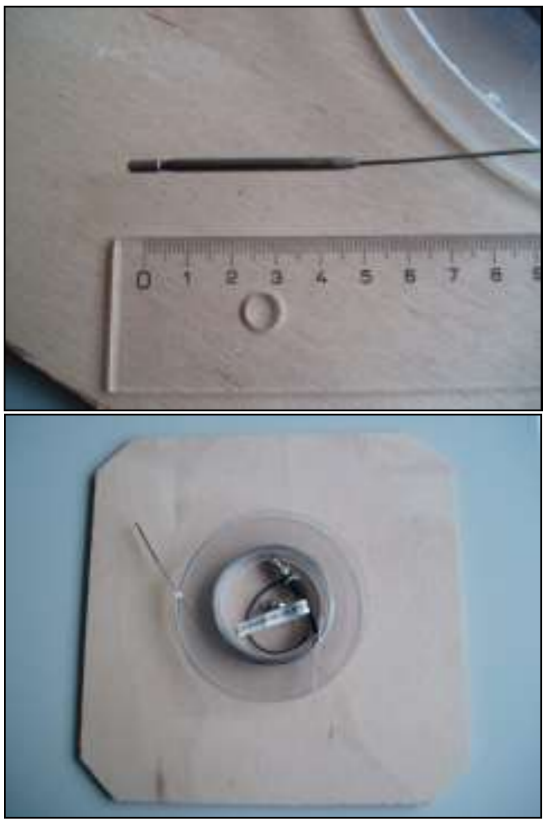

Figure 30: Pictures of the fission chamber model CFUR43/C5B-U8, by Photonis.

Figure 31 shows the mount used by Photonis when testing at its facilities.

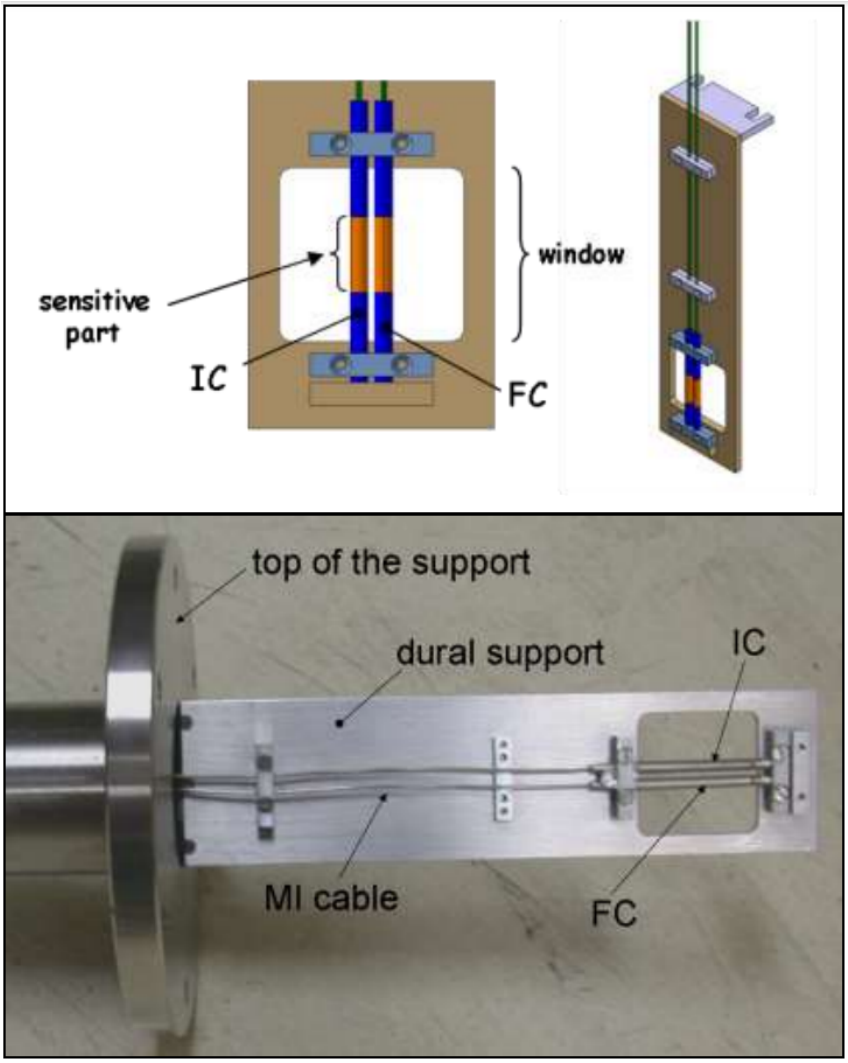

Figure 31: Assembly for Test 1. Part of the mount for supporting the detectors during the irradiation.

4.2.3 Materials of future experiments at UGR facility

The pending task of performing tests 3 and 4 for all (except three) micro cameras will be carried out at the X-ray generator facility of the University of Granada when it is operational. The following materials will then be used:

- Calibration bench T90009, T90014-L, T90015 and T90016-L
- PTW Calibration Facility
- YXLON.TU 320-D03 Bipolar Metal-Ceramic X-Ray Tube
- X-Ray Tube Support T90013
- KeySight Electrometer B2980B Series
- Computers, Reflectometre and Oscilloscope

Below are some photographs of the UGR ray X generator facilities to illustrate the equipment used.

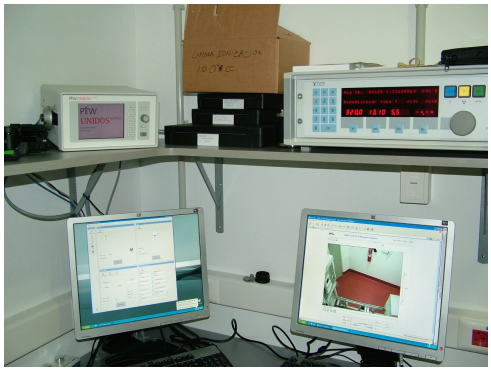

Figure 32: Computers and Amperemeter

Figure 33: PTW Calibration Facility

Figure 34: Calibration bench

All the documentation of this equipment is in the dossier created together with the Jupyter notebooks.

The UGR facilities have the following detectors arranged in the test RIG:

Detector	Qty.	Supply voltage (V)	output signal	Adquisition frequency
MFC - Fast	4	0-400 (150 recom.)	$\approx$ nA (10^{-9} A)	0.2-1 MHz
MFC - Slow	8	0-400 (150 recom.)	$\approx$ nA (10^{-9} A)	2-5 kHz
IC	15	0-400 (150 recom.)	$\approx$ nA (10^{-9} A)	2-5 kHz
SPND	6	N/A	$\approx$ pA (10^{-12} A)	0.1 kHz
Thermocouple	11	N/A	Tenths of mV	1 kHz

Table 3: The different detectors available at the UGR's X-ray generation facilities

These sensors will be installed in an RIG for subsequent irradiation according to the configuration shown in the figure 35.

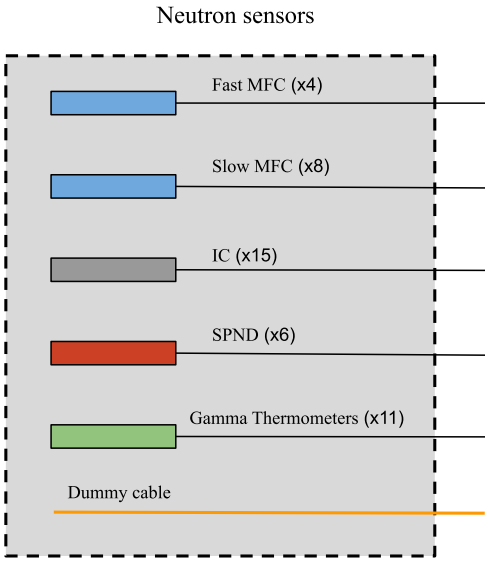

Figure 35: RIG with detectors

Of all the sensors owned by UGR that are listed in table 3 and represented in figure 35, only the MFC-Fast, MFC-Slow and IC are detectors created by Photonis, the rest come from other manufacturers and are not the subject of this work. It can be seen that not all the detectors that Photonis has created are present in this list, the 3 missing detectors are not in UGR's possession and I do not have access to the information regarding their whereabouts.

5 Results and discussion

5.1 Characteristic applied voltage - ionisation current

The behaviour of the detectors within the X-ray beam by varying the applied voltage between their terminals is shown in this subsection, for both ionisation and fission microchambers.

5.1.1 Ionization chambers

Figure 36 shows the data of the 15 micro ionisation chambers to which test number 1 has been performed.

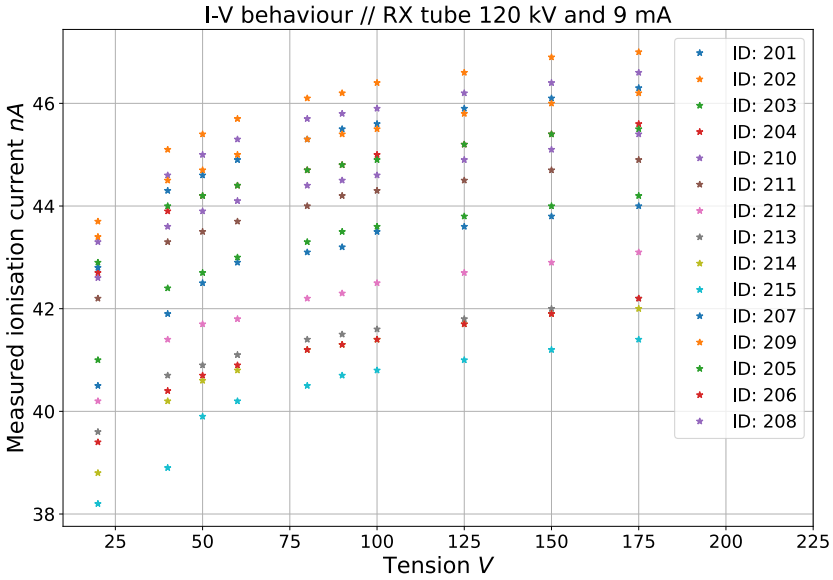

Figure 36: I-V behavior of ionization microchambers.

By applying the criteria mentioned above in the section on methodology, the optimum bias voltage for each detector has been determined from the data shown in figure 36.

The polarisation voltages applying this criterion can be seen in table 4 for each microchamber. All data shown in tables 4 and 6 have been calculated using the python code developed in the Jupyter notebooks.

ID	Polarisation voltage (V)
201	123.33
202	128.03
203	123.33
204	123.33
205	126.46
206	118.63
207	126.46
208	118.63
209	123.33
210	124.89
211	124.89
212	124.89
213	120.20
214	126.46
215	132.72

Table 4: Different polarisation voltages for micro ionisation chambers.

As can be observed in figure 36, the obtained data for the different ionization mi-

crochambers are not coincident. This can be attributed to the fact that, despite establishing tolerances in the manufacturing process, there may be deviations within those tolerances, resulting in differences in the response of the detectors. Furthermore, sensitivity to operating conditions also plays a role. Ionization detectors can be sensitive to operational conditions such as temperature, humidity, and bias voltage. Small variations in these conditions can influence the detector's response and lead to differences in the obtained curves. This also applies, as shown below, to the fission microchambers, where additional variables come into play, such as the amount of fissionable material and the inhomogeneity of the fissionable material layer thickness.

5.1.2 Fission chambers

Figure 37 shows the data of the 9 U^{238} current mode fission microchambers that have been subjected to test number 1.

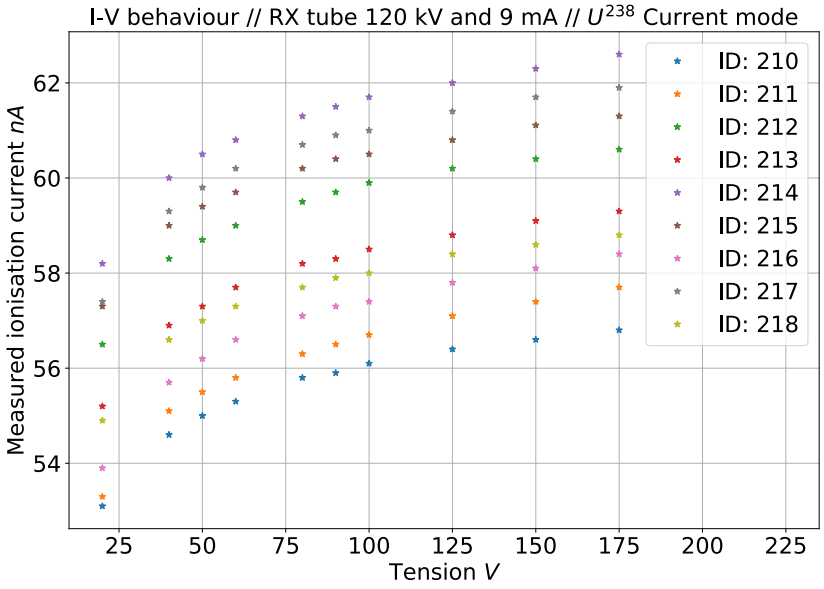

Figure 37: I-V behavior of U^{238} pulse mode fission microchambers.

Figure 38 shows the data of the 3 U^{238} pulse mode fission microchambers that have been subjected to test number 1. Furthermore, a quadratic regression has been performed on the data from this group of microcameras, and the parameters can be found in table 5.

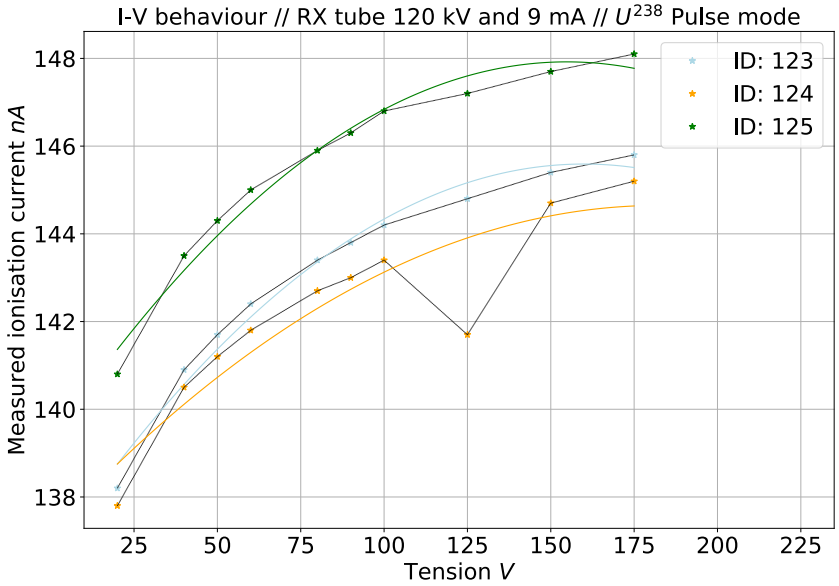

Figure 38: I-V behavior of U^{238} pulse mode fission microchambers with quadratic regression.

ID	123	124	125
a [nA/V^2]	$(-34.9 \pm 5.2) \cdot 10^{-5}$	$(-2.2 \pm 1.4) \cdot 10^{-4}$	$(-36.1 \pm 5.5) \cdot 10^{-5}$
b [nA/V]	0.112 ± 0.010	0.081 ± 0.029	0.112 ± 0.011
c [nA]	136.65 ± 0.45	137.2 ± 1.3	139.27 ± 0.47
R^2	0.98	0.82	0.97

Table 5: Parameters of the quadratic fit of the data represented in figure 38

Figure 39 shows the data of the 3 U^{235} current mode fission microchambers that have been subjected to test number 1.

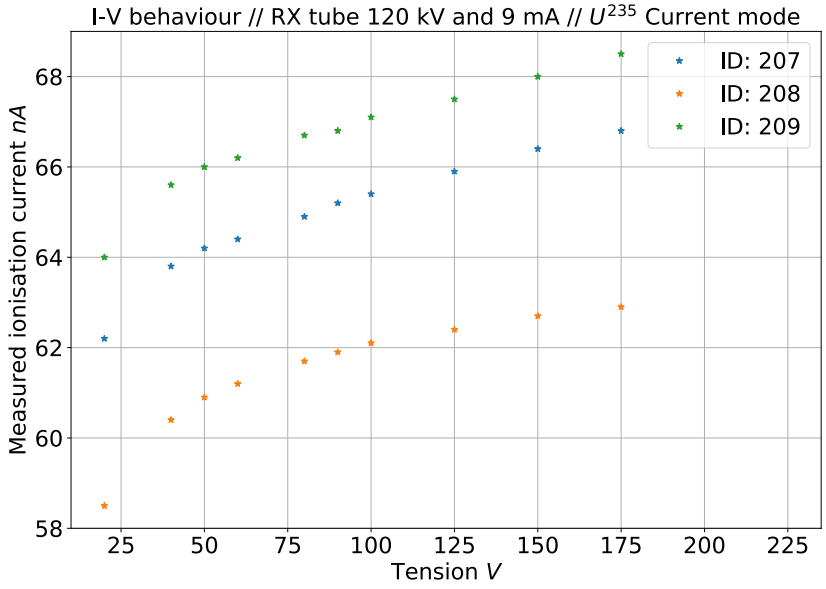

Figure 39: I-V behavior of U^{235} current mode fission microchambers.

Applying the same criteria as for the micro ionisation chambers, the optimum bias voltage for each detector has been determined from the data shown in figures 37, 38 and 39. These data can be found in table 6.

ID	Polarisation voltage (V)
210	128.03
211	123.33
212	128.03
213	124.89
214	123.33
215	124.89
216	123.33
217	124.89
218	124.89
123	134.29
124	107.67
125	132.72
207	121.76
208	124.89
209	115.50

Table 6: Different polarisation voltages for fission microchambers.

As mentioned above, it should be noted that the STUMM-PROTO is capable of biasing all detectors to independent voltages. This is convenient as the optimum polarisation point of each detector is inevitably different due to differences within manufacturing tolerances.

5.2 Characteristic radiation intensity - ionisation current

This subsection shows the behaviour of the detectors within the X-ray beam when the X-ray intensity is varied while the bias voltage of the microchamber is fixed, for both ionisation and fission microchambers.

5.2.1 Ionization chambers

Figure 40 shows the data of the three micro ionisation chambers to which test number 2 has been performed.

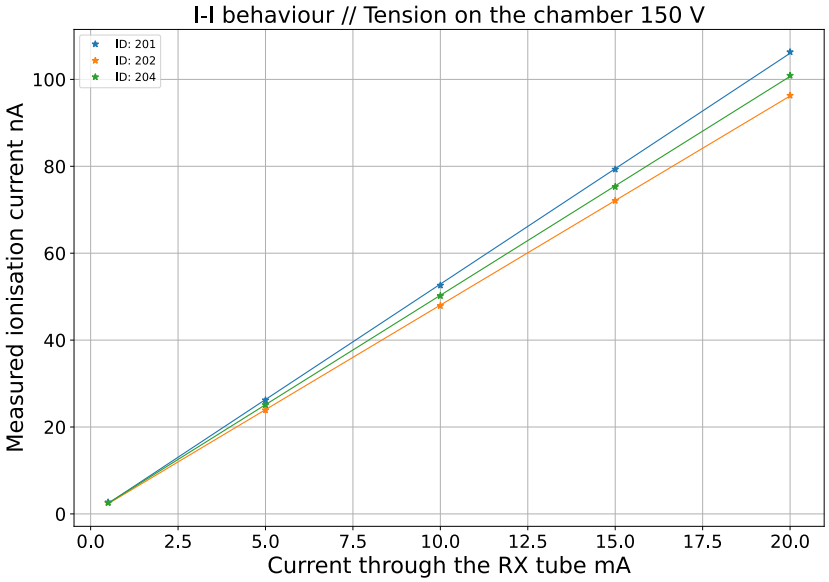

Figure 40: I-I behavior of ionization microchambers with linear regression.

As can be seen, the behaviour of these detectors is linear as the radiation intensity varies. This is because they operate in a saturation regime. It was determined that the bias voltage for this test was 150 V. The parameters of the linear regression for each data set can be seen in table 7. The slope of the line of best fit is a and the ordinate at the origin is b.

ID	201	202	204
a [nA/mA]	5.31 ± 0.02	4.81 ± 0.01	5.04 ± 0.01
b [nA]	-0.24 ± 0.02	-0.07 ± 0.01	-0.05 ± 0.01
Correlation coefficient	0.999997	0.999993	0.999990

Table 7: Linear regression parameters of ionisation microchambers.

It can be seen that the best-fit lines for each detector data have a similar but slightly different slope, which means that the sensitivity of each detector is slightly different. These small differences must be due to the small differences within the manufacturing tolerances of each microchamber, since in essence the three microchambers whose data have been plotted are identical except for deviations within manufacturing tolerances.

5.2.2 Fission chambers

Figure 41 shows the data of the four micro fission chambers to which test number 2 has been performed.

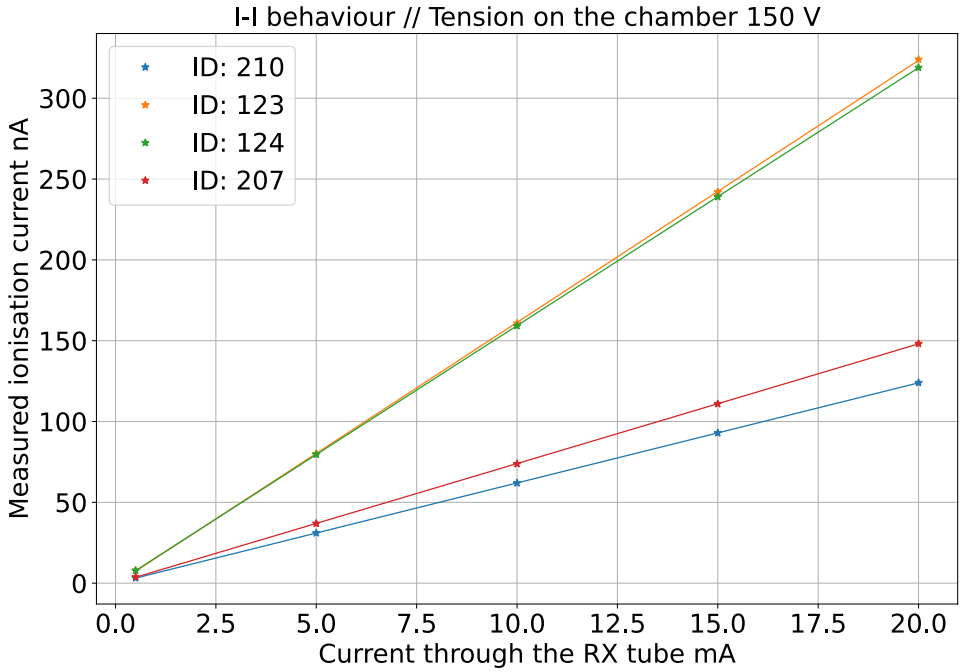

Figure 41: I-I behavior of fission microchambers with linear regression.

The bias voltage was set to 150 V, again in the saturation region. The parameters of the linear regression for each data set can be seen in table 8.

ID	210	123	124	207
a [nA/mA]	6.19 ± 0.01	16.21 ± 0.04	15.96 ± 0.01	7.40 ± 0.01
b [nA]	0.04 ± 0.01	-0.75 ± 0.04	-0.23 ± 0.01	-0.06 ± 0.01
Correlation coefficient	0.999998	0.999990	0.9999996	0.999996

Table 8: Linear regression parameters of fission microchambers.

The differences between the slopes are due to the fact that the four detectors are not of the same group. Detector with ID 207 is an U^{235} current-mode micro fission chamber and detector with ID 210 is a U^{238} current-mode micro fission chamber. Both have a very different slope to the other two microchambers whose data are represented, this is mainly due to the difference in the mode of operation of each pair of microchambers. The current mode is, as can be seen from the data shown, much less sensitive for the same irradiation rate than the pulsed mode. It can be seen that the slope of the line that best fits the data from the two microchambers operating in current mode are slightly different, a contribution to this difference is evidently due to the difference in the type of fissile material these microchambers are made of. The ID 207 microchamber made with U^{235} has a maximum total activity of 1080 Bq, while the 210 has an activity of 12.2 Bq, this difference is key to understand why the slope of the ID 207 microchamber is slightly higher than the ID 210, as the very activity of the Uranium that constitutes the walls of the microchamber contributes to the detection made by the microchamber, thus giving a higher detection for the same intensity of radiation passing through the two microchambers.

On the other hand, the detectors with ID 123 and 124 micro fission chambers are of the pulsed mode type, both with U^{238}, so the slope of the line crossing their data is much more similar between them than the case of the two microchambers (with ID 207 and 210).

5.3 Leakage current and electrical resistance at two temperatures

This subsection displays the electrical characteristics, including resistance and leakage current, of the different microchambers at two different temperatures, 25 and 350 degrees Celsius.

5.3.1 Ionization chambers

Figures 42 and 43 display the electrical characteristics of the ionization microchambers at 25 and 350 °C, respectively.

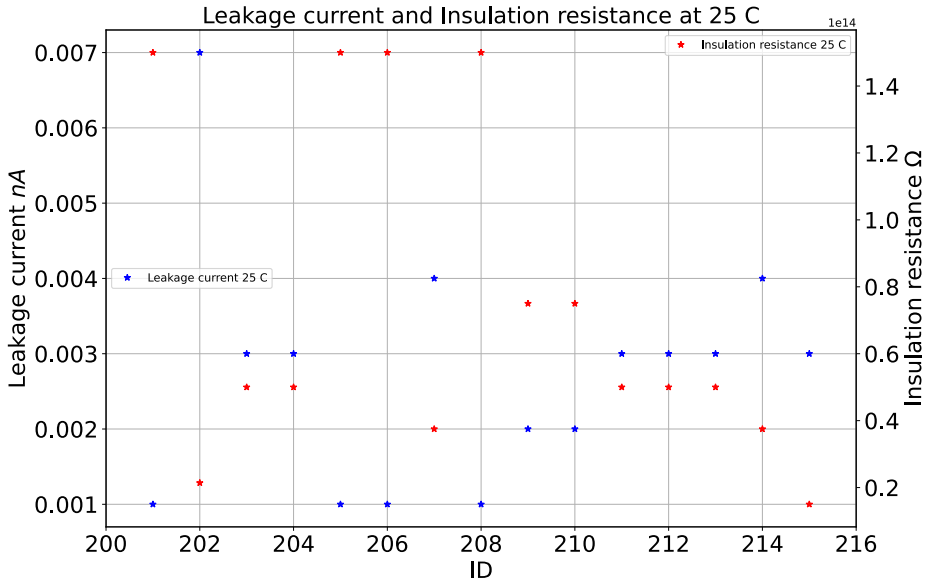

Figure 42: Leakage current and electrical resistance of the IMC at 25 ºC.

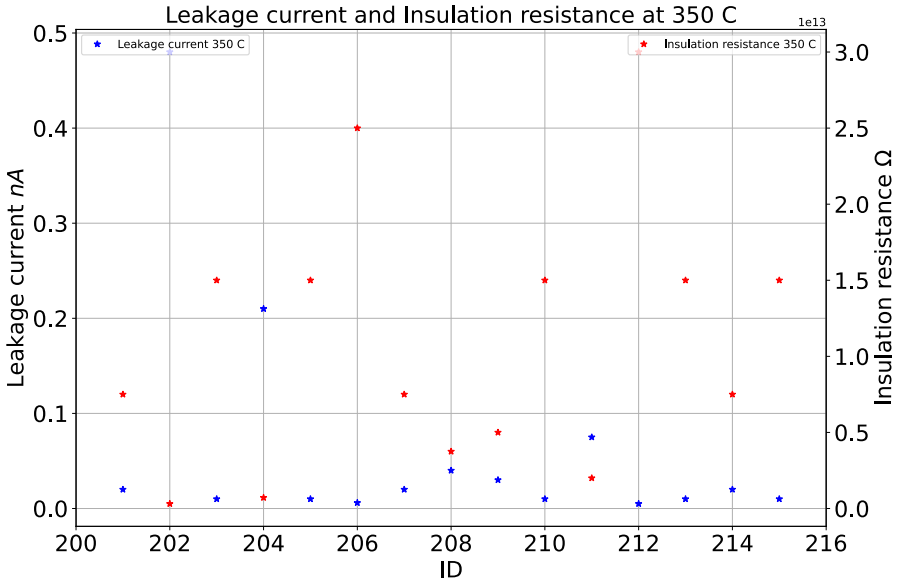

Figure 43: Leakage current and electrical resistance of the IMC at 350 °C.

We observe that the increase in temperature has a direct effect on the leakage current, which generally increases with temperature. However, the increase in leakage current is not the same for all microchambers. For instance, microchamber with ID 202 experiences an increase of 2 orders of magnitude, going from 0.007 nA to 0.48 nA, whereas microchamber with ID 206 increases from 0.001 nA to 0.006 nA.

The electrical resistance generally decreases as the temperature increases, although some microchambers experience a greater decrease of up to one order of magnitude compared to others.

5.3.2 Fission chambers

Figures 44 and 45 display the electrical characteristics of the ionization microchambers at 25 and 350 °C, respectively.

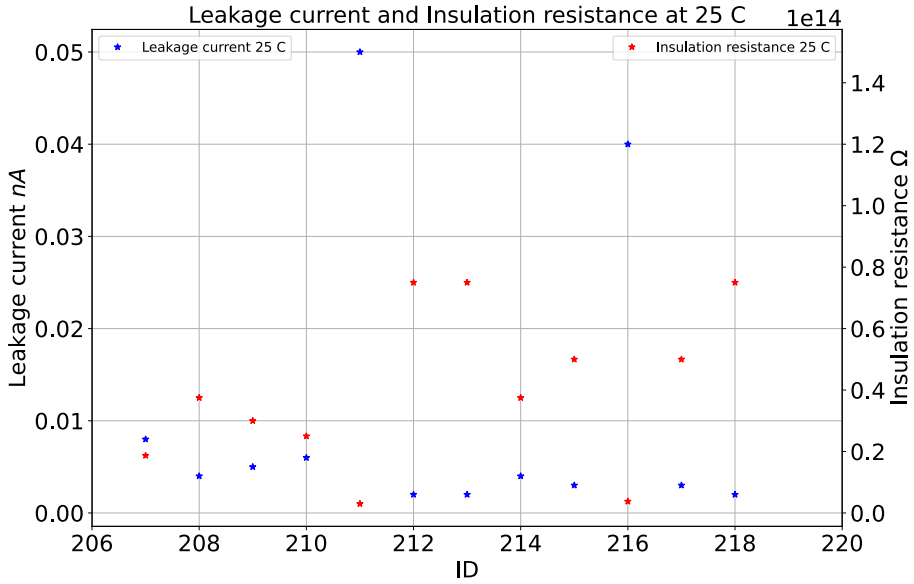

Figure 44: Leakage current and electrical resistance of the FMC at 25 ºC.

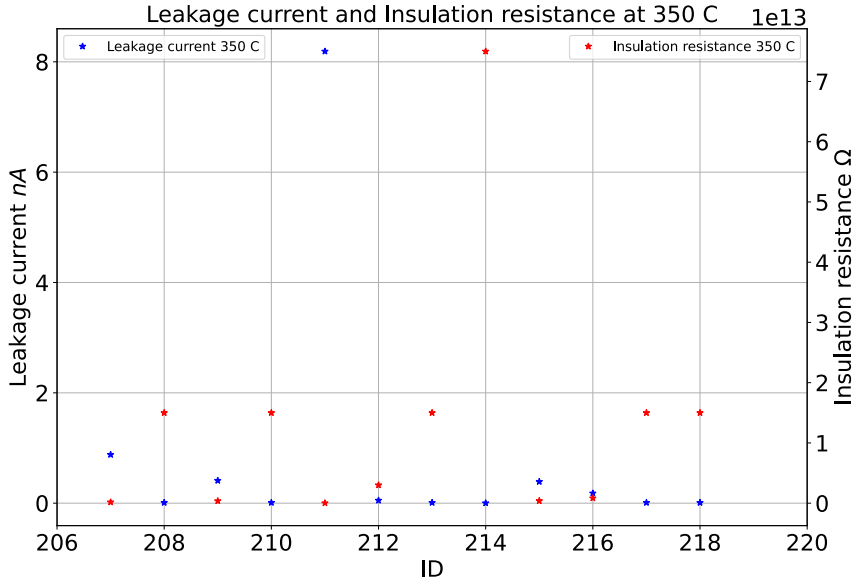

Figure 45: Leakage current and electrical resistance of the FMC at 350 ºC.

We observe that the increase in temperature has a direct effect on the leakage current again, which generally increases with temperature. However, the increase in leakage current is not the same for all microchambers. For instance, microchamber with ID 211 experiences an increase of 2 orders of magnitude, going from 0.05 nA to 8.19 nA, whereas microchamber with ID 210 increases from 0.006 nA to 0.01 nA.

The electrical resistance generally decreases as the temperature increases, although some microchambers experience a greater decrease of up to one order of magnitude compared to others.

The three missing fission microcameras are the ones operating in pulsed mode, which, as seen in figures 46 and 47, exhibit a different magnitude of response compared to those operating in current mode.

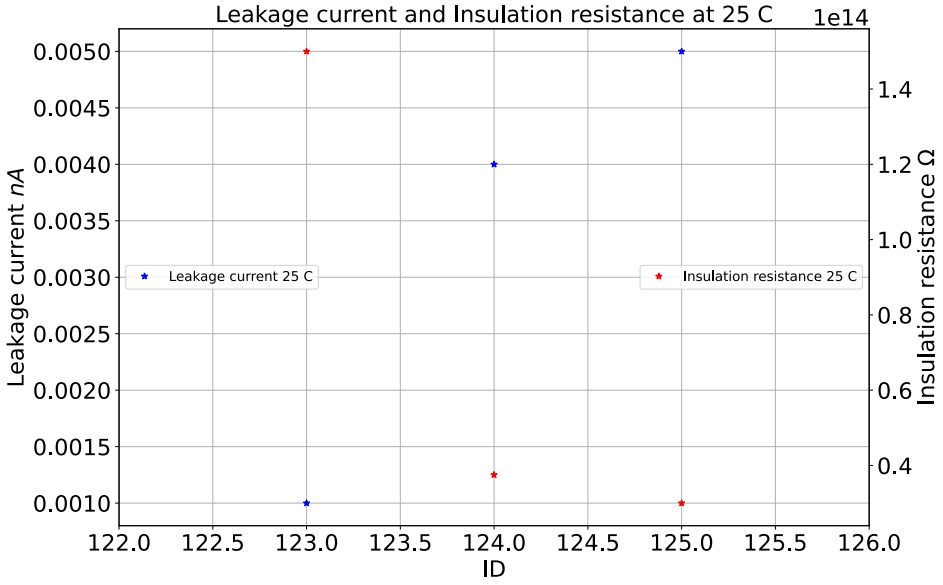

Figure 46: Leakage current and electrical resistance of the FMC at 25 ºC.

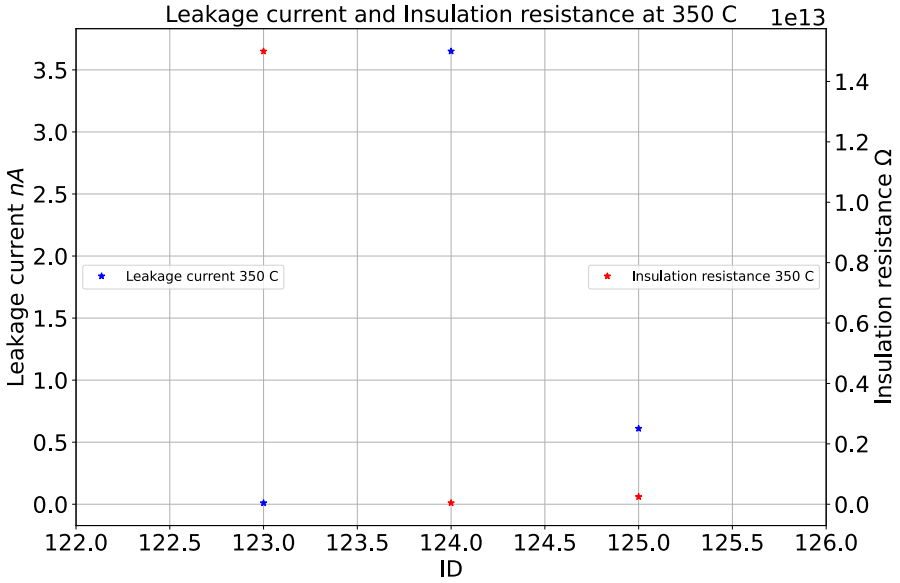

Figure 47: Leakage current and electrical resistance of the FMC at 350 ºC.

As observed, once again the leakage current increases non-uniformly with the temperature. The microcamera with ID 123 goes from 0.001 nA to 0.01 nA, while the microcamera with ID 124 increases from 0.004 nA to 3.65 nA, three orders of magnitude

higher after heating. On the other hand, the electrical resistance decreases in general and non-uniformly as the temperature increases.

5.4 Characteristic applied voltage - ionisation current with volume

When plotting the ionisation intensity versus bias voltage for the different detectors we see that the data sets do not coincide, as mentioned before this is due to small differences in the physical characteristics of the individual detectors which are within the manufacturer's tolerance range. However, if we also indicate the sensitive volume of each detector in this representation, the figure 48 below is the result.

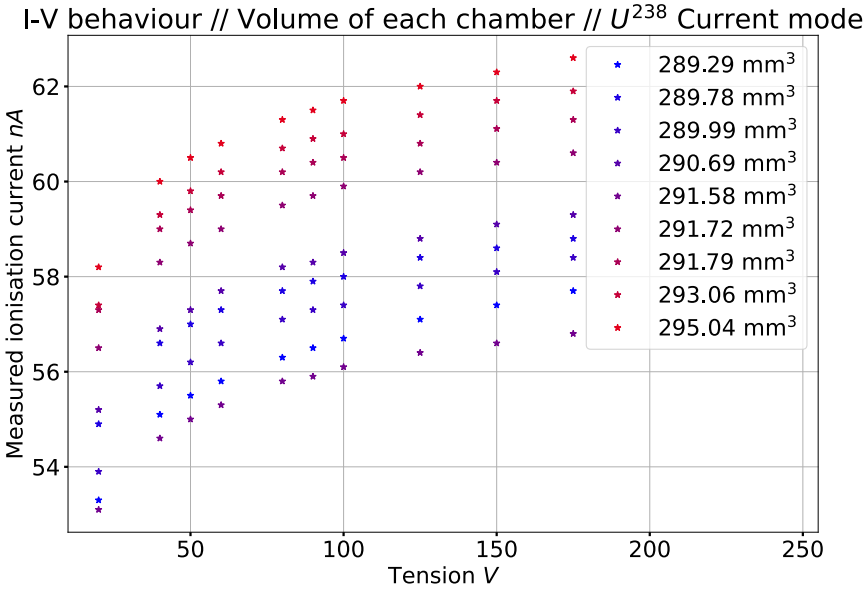

Figure 48: I-V behavior and volume of U^{238} pulse mode FMC.

As can be seen there is an obvious trend, as the microchamber has a higher sensitive volume the response is also higher. This can be seen more clearly in the figure 49.

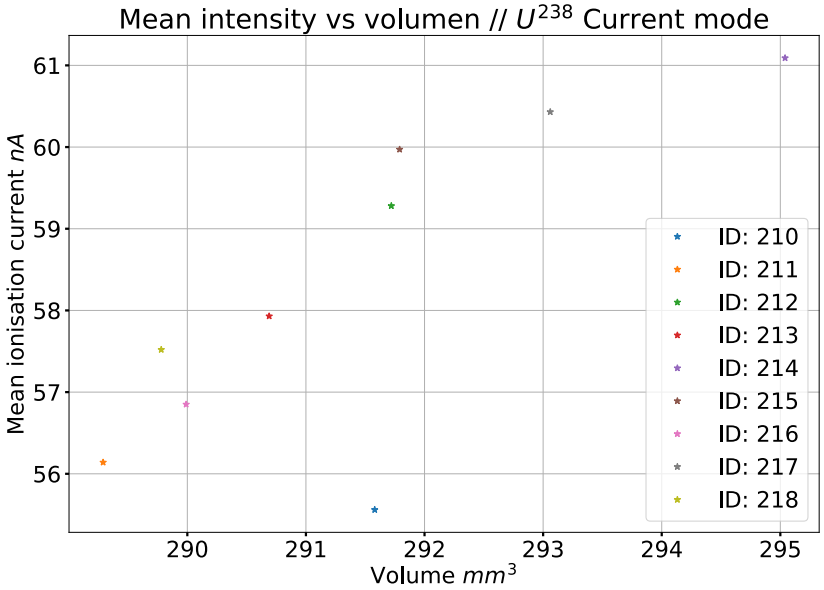

Figure 49: Average intensity as a function of the volumen of each U^{238} current mode FMC.

Interestingly, this behaviour is not seen in the ionisation microchambers, as can be seen in figure 50. This is expected to be due to the difference in fissile material between the two types, one type with U^{238} and the other without.

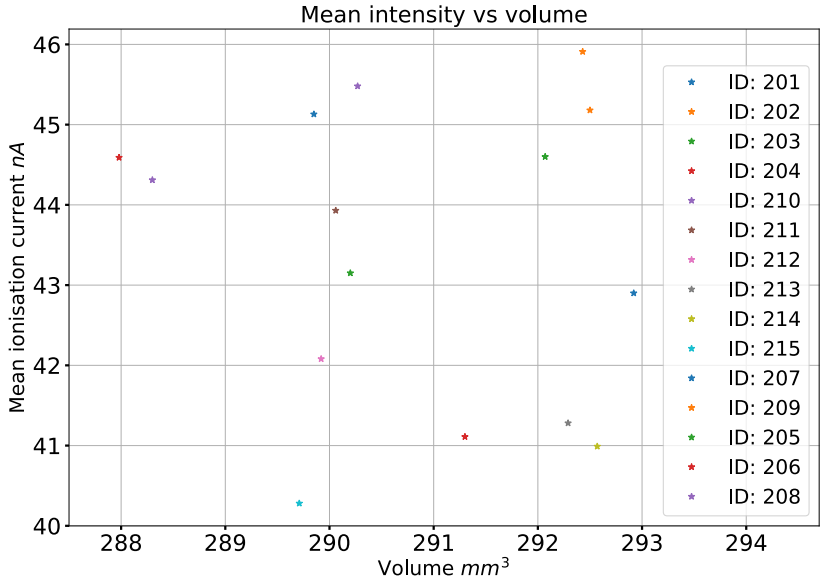

Figure 50: Average intensity as a function of the volumen of each IMC.

Data from the remaining fission microchambers have not been presented because they are divided into two groups of three microchambers each, and have been considered too few chambers to draw general trends.

6 Conclusions

The interest of this work lies in the fact that the neutron sensors studied have been specially manufactured for IFMIF-DONES and are small in size, which makes them unique in their type. These detectors are expected to characterize the radiation beam generated in IFMIF-DONES, which consists of a neutron beam with a flux of $10^{14}\ \frac{n}{cm^2\ s}$ and a peak energy of 14 MeV, as well as a photon beam with a different intensity and energy than the one used in the factory acceptance by Photonis. The analysis conducted in this work is based on data obtained solely from photon irradiation, with characteristics that differ from those expected in IFMIF-DONES. Therefore, no predictions can be made regarding their ability to efficiently characterize the neutron radiation beam in IFMIF-DONES. Nevertheless, the data obtained from measurements at the manufacturer's facilities provide valuable information on the response of the sensors to photons radiation and their detection capability.

6.1 Conclusions test 1

Through the acceptance process at the manufacturer's facilities, the optimum bias voltage has been determined from the data from test 1. It is expected that each microchamber will be powered individually for an optimum result. The optimal polarisation of the microchambers can be found in tables 4 and 6 for ionization and fission microchambers.

The optimal bias voltage of the fission microchamber with ID 124 deviates anomalously from the trend observed within its own group. By examining figure 38, we can identify an anomalous data point. As a result, it is being considered to discard the result of this test for the microchamber with ID 124. It is proposed to repeat test 1 for this microchamber at the UGR facilities to evaluate whether the result is valid or invalid.

6.2 Conclusions test 2

The ionization and fission microchambers manufactured for the radiation levels expected in IFMIF-DONES have been found to behave linearly in test number 2, this means that the response of the detector is linear with the variation of the intensity of the radiation passing through it, as we can see in figures 40 and 41.

The behavior has been determined to be linear, as the linear correlation coefficient differs from unity by less than one ten-thousandth for all the tested detectors. This confirms that the detectors are valid for reliably characterizing the X-ray beam used in Photonis.

6.2.1 Fission microchambers

The data from the fission microchambers reveal two distinct linear behaviors, corresponding to the two operating modes of the fission microchambers: current mode

and pulsed mode. Among the two modes, the pulsed mode exhibits more variation in response for the same change in the applied external stimulus. Initially, the goal is to achieve the highest stimulus-response relationship, making the detectors in pulsed mode appear more optimal. However, the pulsed mode comes with drawbacks that must be considered as they hinder its proper operation under a sufficiently intense radiation beam.

As discussed in the theoretical framework, the pulsed mode is designed to detect singular events, and its correct functioning requires that the intensity pulses produced in the detector do not overlap. This directly relates to the intensity of the radiation beam and the characteristic discharge time of the circuit connected to the detector. The photon beam intensity used by Photonis appears to be sufficiently low for the detectors operating in pulsed mode to exhibit the expected linear behavior.

Based on the obtained data, it is not possible to predict whether these same detectors (operating in pulsed mode) will maintain their linear behavior in IFMIF-DONES due to differences in intensity and equipment coupled to the detector.

Furthermore, the detectors operating in current mode also exhibit linear behavior. The current mode allows them to detect higher radiation intensities under the same circumstances as those operating in pulsed mode.

6.2.2 Ionization microchambers

The linear behavior in the ionization microchambers does not differentiate between multiple groups, as expected. This implies that their behaviors are sufficiently similar to not exhibit anomalous behaviors.

6.3 Conclusions test 5

For both ionization microcameras and fission cameras, some general trends can be observed. These are:

- The leakage current increases as the temperature rises.
- The electrical resistance decreases as the temperature increases.

These trends do not accurately reflect the behavior of each individual detector, as we observe significant diversity in their responses. Some microcameras exhibit an increase in leakage current by one order of magnitude, while others show an increase of up to three orders of magnitude. Similarly, the electrical resistance displays unique patterns of decrease.

6.4 Conclusion voltage - ionisation current with volume

The data presented in figure 49 exhibits a clear upward trend of average intensity as the volume of the fission microchamber increases. This emerging behavior should be taken into account at an individual level when using fission microchambers to characterize radiation. It is worth noting that this trend does not occur with ionization

microchambers as seens in figure 50.

In the near future, the missing tests will have to be performed at the UGR facilities to complete the data set and determine whether or not they are valid for detecting the expected radiation in IFMIF-DONES.

7 Bibliography

[1] L.A. Banda and B. I. Nappi, IEEE Trans. Nucl. Sci. NS-23(1), 311 (1976).

[2] H. Bock and M. Stimler, Nucl. Instrum. Meth. 87, 299 (1970).

[3] H. Bock, Nucl. Instrum. Meth. 125, 327 (1975).

[4] Certificates of activity of the devices.

[5] CIEMAT folleto imagen nuevo. Available at: `http://www-fusion.ciemat.es/media/20150622_FOLLETO_LNF_pre.pdf`

[6] "Design Status and Main Achievements Within the EUROfusion FP8 Work Programme". The IFMIF-DONES Project. Oct. 2022. *Journal of Fusion Energy*.

[7] Factory acceptance dossiers.

[8] "Feasibility of fission chambers as a neutron diagnostic in the IFMIF-Test Cell". Mar. 2009.

[9] Fiore, M. "Neutron diagnostics for the IFMIF-DONES Test Cell". PhD thesis, diaFusion, 2021.

[10] IFMIF International Team. "IFMIF Comprehensive Design Report (CDR)". IAEA Report. Dec. 2003.

[11] IFMIF-CDA-Team. "IFMIF - Conceptual Design Activity Final Report". In: ENEA-RT/ERG/FUS/9611-Report, ed. by M. Martone. Dec. 1996.

[12] IFMIF-DONES documentation.

[13] Steinmeyer, Paul R. "Ion Chambers: Everything You've Wanted to Know (But Were Afraid to Ask)". *RSO Magazine*. Vol. 8, no. 5. 2003.

[14] Knoll, Glenn F. *Radiation Detection and Measurement*. John Wiley & Sons, 2010.

[15] R. T. Kouzes et al., Nucl. Instrum. Meth. A587, 89 (2008).

[16] J. C. Kroon, F. M. Smith, and R. I. Taylor, Trans. Am. Nucl. Soc. 23, 459 (1976).

[17] W. Lee et al., IEEE Trans. Nucl. Sci. 48(4), 1587 (2001).

[18] G. F. Lynch, R. B. Shields, and P. G. Coulter, IEEE Trans. Nucl. Sci. NS-24(1), 692 (1977)

[19] A. K. Mahant, P. S. Rao, and S. C. Misra, Nucl. Instrum. Meth. A406, 117 (1998).

[20] Martin, Jose Antonio. "Fusión Nuclear: IFMIF-DONES en Granada". Jan. 2019. Available at: https://joseantoniomartin.wordpress.com/2019/01/27/fusion-nuclear-ifmif-dones-en-granada/

[21] R. Van Nieuwenhove, Nucl. Instrum. Meth. A373, 202 (1996).

[22] Podgoršak, E.B. Radiation Oncology Physics, (2005a).

[23] P. S. Rao and S. C. Misra, Nucl. Instrum. Meth. A253, 57 (1986).

[24] Reports of past irradiation experiments with ionization and fission microchambers.

[25] W. Seifritz, Nucl. Sci. Eng. 49, 358 (1972).

[26] R. B. Shields, IEEE Trans. Nucl. Sci. NS-20(1), 603 (1973)

[27] H. H. Stevens,"Neutron Sensors-In-Core," Chap. 3 in Nuclear Power Reactor Instrumentation Systems Handbook, TID-25952-Pl (1973)

[28] H. R. Vega-Carrillo and E. Manzanares-Acuna, Nucl. Instrum. Meth. A524, 146 (2004).

[29] P. Gebureck et al., IAEA-SM-168/G-8, p. 783 (1973).

[30] P. Goldhagen et al., Nucl. Instrum. Meth. A476, 42 (2002).

[31] N. P. Goldstein, IEEE Trans. Nucl. Sci. NS-20(1), 549 (1973)

[32] N. P. Goldstein, IEEE Trans. Nucl. Sci. NS-25(1), 292 (1978).

[33] N. P. Goldstein, C. L. Chen, and W. H. Todt, IEEE Trans. Nucl. Sci. NS-28(1), 752 (1981)